

BESIII Analysis Memo

BAM-xxx

February 11, 2025

Study of $\psi(3686) \rightarrow \Lambda \bar{\Lambda} \pi^0$ and $\psi(3686) \rightarrow \Lambda \bar{\Lambda} \eta$

Peng Zhang^{a,b}, Shuangshi Fang^b, Fang Liu^b, Daihui Wei^b, and Liqing Qin^a^a*Guangxi Normal University*^b*Institute of High Energy Physics*

Referee Committee

Referee A (Chair)^d, Referee B^e, Referee C^f^d*Uni D*^e*Uni E*^f*Uni F*

Pubcomm Editors

Editor B

HN : <http://hnbess3.ihep.ac.cn/HyperNews/get/paperxxx.html>

Abstract

Using $(2712 \pm 14) \times 10^6$ $\psi(3686)$ events collected with the BESIII detector, the decays of $\psi(3686) \rightarrow \Lambda \bar{\Lambda} \pi^0$ and $\psi(3686) \rightarrow \Lambda \bar{\Lambda} \eta$ are studied. The branching fraction of $\psi(3686) \rightarrow \Lambda \bar{\Lambda} \pi^0$ is determined to be $(0.93 \pm 0.15 \pm 0.08) \times 10^{-6}$. The partial wave analysis of $\psi(3686) \rightarrow \Lambda \bar{\Lambda} \eta$ is also performed, and there are three intermediate resonances $\Lambda(1670)$, $\Lambda(1800)$, and $\Lambda(2110)$ in the $\Lambda \eta$ system. The branching fraction of $\psi(3686) \rightarrow \Lambda \bar{\Lambda} \eta$ is determined to be $(2.43 \pm 0.07 \pm 0.17) \times 10^{-5}$, the branching fractions of three intermediate resonances are measured for the first time to be $(0.91 \pm 0.06 \pm 0.12) \times 10^{-5}$, $(0.32 \pm 0.12 \pm 0.06) \times 10^{-5}$, and $(0.46 \pm 0.05 \pm 0.07) \times 10^{-5}$, respectively.

An evident structure around the $\Lambda \bar{\Lambda}$ mass threshold is observed for the first time in $\psi(3686) \rightarrow \Lambda \bar{\Lambda} \eta$. In accordance with the amplitude analysis, its mass and width are determined to be $(2291 \pm 5 \pm 6.3) \text{ MeV}/c^2$ and $(25 \pm 8 \pm 7.0) \text{ MeV}$, respectively, and the spin favors 1^{--} , where the first uncertainties are statistical and the second systematic.

27 Contents

28	1 Introduction	2
29	2 BESIII Detector	3
30	3 Data Sample and Monte Carlo Simulation	4
31	4 Event Selection	5
32	5 Analysis of $\psi(3686) \rightarrow \Lambda \bar{\Lambda} \pi^0$	6
33	5.1 Final Event Selection	6
34	5.2 Background estimation	8
35	5.2.1 Hadronic background	9
36	5.2.2 QED continuum background	10
37	5.3 Mass Spectrum Fitting	11
38	5.4 Branching Fraction Calculation	11
39	6 Partial wave analysis of $\psi(3686) \rightarrow \Lambda \bar{\Lambda} \eta$	12
40	6.1 Final Event Selection	12
41	6.2 Background estimation	14
42	6.3 Mass Spectrum Fitting	15
43	6.4 Partial wave analysis	16
44	6.4.1 Data Distribution	16
45	6.4.2 Background Treatment	16
46	6.5 PWA method	17
47	6.6 Likelihood function construction and fit fraction	19
48	6.7 PWA solution	20
49	6.7.1 Baseline solution	20
50	6.7.2 IO check	22
51	6.8 Branching Fraction Calculation	23
52	7 Study of Enhancement near $\Lambda \bar{\Lambda}$ Mass Threshold	23
53	7.1 Possible Exotic State	23
54	7.2 Theoretical Models and Experimental Results.	25

55	8 Systematic Uncertainties	26
56	8.1 $\psi(3686) \rightarrow \Lambda \bar{\Lambda} \pi^0$ systematic uncertainties	27
57	8.2 $\psi(3686) \rightarrow \Lambda \bar{\Lambda} \eta$ systematic uncertainties	29
58	9 Summary	32
59	10 Appendices	35

60 1 Introduction

61 Excited baryons with light valence quarks (u, d, s) contain the information for understanding the non-
 62 perturbative aspects, confinements and chiral symmetry breaking, of Quantum Chromodynamics. The
 63 excited baryons are unstable and couple **with meson-baryon continuum states** to form hyperon resonances
 64 (Λ^*) with $S = -1$. Thus the extraction of these baryon resonances from the data of hadron-, photon-and
 65 electron-induced meson production reactions has long been an important task in the hadron physics.
 66 However, the hyperon resonances are much less understood than the nucleon resonances. We study
 67 the behavior with the number of colors (N_c) of the $\Lambda(1670)$ resonances obtained dynamically within
 68 the chiral unitary approach [1]. The leading order meson-baryon interaction, used as the kernel of the
 69 unitarization procedure, manifests a nontrivial N_c dependence of the flavor SU(3) representation for
 70 baryons.

71 Enhancements near the baryon-antibaryon mass threshold have been observed in various experi-
 72 ments, including low-energy $p\bar{p}$ collisions, charmonium decays, and B meson decays. These observa-
 73 tions have attracted significant interest as they suggest the possible presence of resonant states in the
 74 vicinity of the threshold. In low-energy $p\bar{p}$ collisions, a structure near the $\Lambda \bar{\Lambda}$ mass threshold was ob-
 75 served through a partial wave analysis of $p\bar{p} \rightarrow \Lambda \bar{\Lambda}$ in PS185 data [2], with a mass of $(2290 \pm 20) \text{ MeV}/c^2$
 76 and a width of $(275 \pm 35) \text{ MeV}$. In charmonium decays, enhancements are reported in several final states,
 77 including $J/\psi \rightarrow \gamma p\bar{p}$, $e^+e^- \rightarrow K^+K^-$, $e^+e^- \rightarrow \Lambda \bar{\Lambda}$, and $e^+e^- \rightarrow \Lambda \bar{\Lambda} \eta$ [3–6]. Similarly, in B me-
 78 son decays, enhancements have been found in the processes $B^0 \rightarrow \Lambda \bar{\Lambda} K^0(K^{*0})$ and $B^0 \rightarrow p \bar{\Lambda} \pi^-$ [7, 8].
 79 These results provide compelling evidence for the existence of resonant states near the baryon-antibaryon
 80 threshold across multiple channels.

81 To explain these observed enhancements, several theoretical models have been proposed. A vector
 82 hexaquark state [9] decaying into $\Lambda \bar{\Lambda}$ has been suggested, with a mass of $2300 \text{ MeV}/c^2$ and a width of
 83 33 MeV . This model proposes that the enhancements may be attributed to a hexaquark configuration that
 84 couples to the $\Lambda \bar{\Lambda}$ system. In the framework of QCD sum rules [10], an investigation of light baryonium
 85 states predicts possible resonant states, including a $\Lambda \bar{\Lambda}$ state with quantum numbers $J^{PC} = 1^{--}$, with a

mass of $(2340 \pm 120) \text{ MeV}/c^2$. In the modified vector meson dominance (VMD) model [11], the mass of the new state in the $e^+e^- \rightarrow \Lambda\bar{\Lambda}$ reaction is predicted to be around 2231 MeV, very close to the $\Lambda\bar{\Lambda}$ mass threshold, with a width of only a few MeV. These theoretical predictions provide a strong foundation for understanding the nature of the observed enhancements.

Experimental measurements have provided crucial data on the mass and width of these enhancements. For instance, in the process $e^+e^- \rightarrow \eta\Lambda\bar{\Lambda}$ [12], the measured values are a mass of $(2356 \pm 7 \pm 15) \text{ MeV}/c^2$ and a width of $(304 \pm 28 \pm 54) \text{ MeV}$. Similarly, in the process $e^+e^- \rightarrow \phi\Lambda\bar{\Lambda}$ [13], the measured mass and width are $(2262 \pm 4 \pm 28) \text{ MeV}/c^2$ and $(72 \pm 5 \pm 43) \text{ MeV}$, respectively. These results provide direct evidence for the resonant structures near the $\Lambda\bar{\Lambda}$ threshold and, while consistent with theoretical predictions regarding their presence, reveal significant deviations in the measured widths compared to theoretical expectations.

In this work, the decays of $\psi(3686) \rightarrow \Lambda\bar{\Lambda}\pi^0$ and $\psi(3686) \rightarrow \Lambda\bar{\Lambda}\eta$ are analysed with seven times data sample of previous work of BESIII [14] to search for the Λ excited baryons and the mass threshold enhancement of $\Lambda\bar{\Lambda}$.

2 BESIII Detector

The BESIII detector [15] records symmetric e^+e^- collisions provided by the BEPCIII storage ring [16] in the center-of-mass energy range from 1.84 to 4.95 GeV, with a peak luminosity of $1.1 \times 10^{33} \text{ cm}^{-2}\text{s}^{-1}$ achieved at $\sqrt{s} = 3.773 \text{ GeV}$. BESIII has collected large data samples in this energy region [17]. The cylindrical core of the BESIII detector covers 93% of the full solid angle and consists of a helium-based multilayer drift chamber (MDC), a time-of-flight system (TOF) and a CsI(Tl) electromagnetic calorimeter (EMC) which are all enclosed in a superconducting solenoidal magnet providing a 1.0 T magnetic field. The magnetic field was 0.9 T in 2012. The solenoid is supported by an octagonal flux-return yoke with resistive plate counter muon identification modules interleaved with steel. The charged-particle momentum resolution at 1 GeV/c is 0.5%, and the dE/dx resolution is 6% for electrons from Bhabha scattering. The EMC measures photon energies with a resolution of (2.5%)(5)% at 1 GeV in the barrel (end cap) region. The time resolution in the plastic scintillator TOF barrel region is 68 ps, while that in the end cap region is 110 ps. The end cap TOF system was upgraded using multigap resistive plate chamber technology in 2015, providing a time resolution of 60 ps, which benefits 5% of the data used in this analysis [18].

3 Data Sample and Monte Carlo Simulation

Both data and Monte Carlo samples are reconstructed in the framework of BESIII Offline Software System(BOSS). The BOSS version used in this analysis is 7.0.9. The following data and Monte Carlo samples are used in this analysis:

- Data:

A total of $(2712.4 \pm 14.3) \times 10^6$ $\psi(3686)$ events were collected at $\sqrt{s} = 3.686$ GeV, including $(107.7 \pm 0.6) \times 10^6$ events taken in 2009, $(345.4 \pm 2.6) \times 10^6$ events in 2012, and $(2259.3 \pm 11.1) \times 10^6$ events [19] in 2021.

Corresponding to an integrated luminosity of $(20,274.8 \pm 42.1)$ pb^{-1} for the full dataset, which is used to study continuous backgrounds, were taken at $\psi(3770)$ with $\sqrt{s} = 3.773$ GeV. This includes data from 2010-2011 with $(2931.8 \pm 0.2 \pm 13.8)$ pb^{-1} , from 2022 with (4995 ± 19) pb^{-1} , from 2023 with (8157 ± 31) pb^{-1} , and from 2024 with (4191 ± 16) pb^{-1} [20, 21].

- Monte Carlo:

Simulated samples produced with the GEANT4-based [22] Monte Carlo (MC) package which includes the geometric description of the BESIII detector and the detector response, are used to determine the detection efficiency and estimate the backgrounds. The simulation includes the beam energy spread and initial state radiation (ISR) in the e^+e^- annihilations modeled with the generator KKMC [23, 24].

The inclusive Monte Carlo sample of 2747 million $\psi(3686)$ events is used to investigate potential background. The sample includes the production of the $\psi(3686)$ resonance and continuous processes incorporated in KKMC. The known decay modes are modeled with EVTGEN [25, 26] using branching fractions taken from the Particle Data Group (PDG) [27], and the remaining unknown decays from the charmonium states with LUNDCHARM [28, 29]. The final state radiation (FSR) from charged final state particles is incorporated with the PHOTOS [30] package.

The generators of the Exclusive Monte Carlo sample are listed in Table 1.

- A phase space MC sample of 2.7×10^6 $\psi(3686) \rightarrow \Lambda \bar{\Lambda} \pi^0$ and $\psi(3686) \rightarrow \Lambda \bar{\Lambda} \eta$ events are simulated to estimated the detection efficiency and integral MC cross section for partial wave analysis(PWA), respectively.
- A signal MC sample of 1.35×10^6 $\psi(3686) \rightarrow \Lambda \bar{\Lambda} \eta$ events is generated with the PWA result to determine signal efficiency and check the validation of PWA result.
- A phase space MC sample of 1.0×10^8 $\psi(3686) \rightarrow \Sigma^0 \bar{\Lambda} \pi^0 + c.c.$ events is generated with the PWA fit result to estimate background.

- A phase space MC sample of 1.35×10^6 $\psi(3686) \rightarrow \bar{\Lambda}\Sigma^+\pi^- + c.c.$ events is generated for background study.

Decay Chain	Generated Events	Generator
$\psi(3686) \rightarrow \Lambda\bar{\Lambda}\pi^0, \Lambda \rightarrow p\pi^-, \bar{\Lambda} \rightarrow \bar{p}\pi^+, \pi^0 \rightarrow \gamma\gamma$	2.7×10^6	PHSP, HYPWK, HYPWK, PHSP
$\psi(3686) \rightarrow \Lambda\bar{\Lambda}\eta, \Lambda \rightarrow p\pi^-, \bar{\Lambda} \rightarrow \bar{p}\pi^+, \eta \rightarrow \gamma\gamma$	2.7×10^6	PHSP, HYPWK, HYPWK, PHSP
$\psi(3686) \rightarrow \Lambda\bar{\Lambda}\eta, \Lambda \rightarrow p\pi^-, \bar{\Lambda} \rightarrow \bar{p}\pi^+, \eta \rightarrow \gamma\gamma$	1.35×10^6	PWA Result
$\psi(3686) \rightarrow \Sigma^0\bar{\Lambda}\pi^0 + c.c., \Sigma^0 \rightarrow \gamma\Lambda, \bar{\Lambda} \rightarrow \bar{p}\pi^+, \pi^0 \rightarrow \gamma\gamma$	1.0×10^8	PWA Result
$\psi(3686) \rightarrow \bar{\Lambda}\Sigma^+\pi^- + c.c., \Sigma^+ \rightarrow p\pi^0$	1.35×10^6	PHSP, PHSP, PHSP, PHSP

Tab. 1: Exclusive MC samples.

4 Event Selection

In this analysis, the decay $\psi(3686) \rightarrow \Lambda\bar{\Lambda}\pi^0(\eta)$ is selected by reconstructing one $\Lambda\bar{\Lambda}$ pair and one $\pi^0(\eta)$ meson, where $\Lambda(\bar{\Lambda})$ candidate is reconstructed by $p\pi^-(\bar{p}\pi^+)$ pair and $\pi^0(\eta)$ candidate is reconstructed from two photons. Each candidate event is required to contain at least four good charged tracks with net zero charge, and at least two photon. The MDC provides reconstruction of charged tracks within $|\cos\theta| < 0.93$, where θ is the polar angle with respect to the beam direction. The charged tracks of the distance of closest approach to the interaction point (IP) must be less than 10 cm along the beam direction and less than 1 cm in the perpendicular to the beam. No particle identification for charged tracks is imposed.

Photon candidates are identified using isolated showers in the EMC. The deposited energy of each shower must be more than 25 MeV in the barrel region ($|\cos\theta| < 0.80$) and more than 50 MeV in the end cap region ($0.86 < |\cos\theta| < 0.92$). The angle subtended by the EMC shower and the position of the closest charged track at the EMC must be greater than 10 degrees as measured from the IP. The difference between the EMC time and the event start time is required to be within $[0, 700]$ ns, is used to suppress electronic noise and showers unrelated to the event.

The $\Lambda(\bar{\Lambda})$ candidates are reconstructed by fulfilling a secondary vertex fit to the pairs of $p(\bar{p})$ and oppositely charged π . Events with at least one Λ and one $\bar{\Lambda}$ candidate are selected when looping over all the combinations of Λ and $\bar{\Lambda}$ candidates, the one with the minimum value of $\chi^2_{s vtx}(\Lambda) + \chi^2_{s vtx}(\bar{\Lambda})$ is chosen, where $\chi^2_{s vtx}(\Lambda)$ and $\chi^2_{s vtx}(\bar{\Lambda})$ are the fit qualities of the secondary vertex fits for Λ and $\bar{\Lambda}$, respectively. No more criteria on the decay length of the second vertex fit for the $\Lambda/\bar{\Lambda}$ candidates is used. A four-constraint energy momentum conservation kinematic fit (4C fit) is performed under the $\Lambda\bar{\Lambda}\gamma\gamma$

hypothesis. If there is more than two photon candidate in an event, the combination with the smallest χ_{4c}^2 is retained.

5 Analysis of $\psi(3686) \rightarrow \Lambda \bar{\Lambda} \pi^0$

5.1 Final Event Selection

- The χ_{4C}^2 distribution between data and MC is shown in Fig. 1, and is further required to be less than 15.

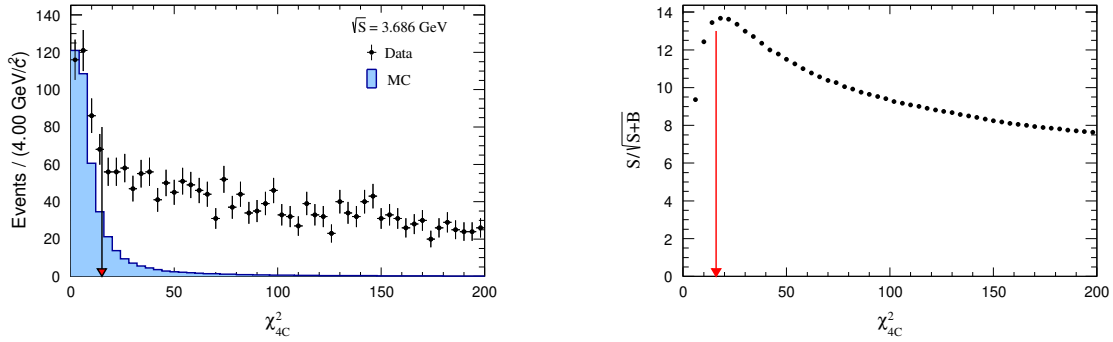


Fig. 1: The distributions of χ_{4C}^2 distribution (left) and optimization of χ_{4C}^2 (right). The dots represent the data sample while the histogram with a blue solid line represents the signal MC sample, which has been normalized to match the data sample.

- The mass spectra of $M(\bar{p}\pi^+)$ and $M(p\pi^-)$ between data and MC are shown in Fig. 2. The $p\pi^-$ invariant mass is required to be in the Λ mass region, $|M(p\pi^-) - M(\Lambda)| < 5 \text{ MeV}/c^2$, where $M(\Lambda)$ is the PDG [27] mass of Λ .

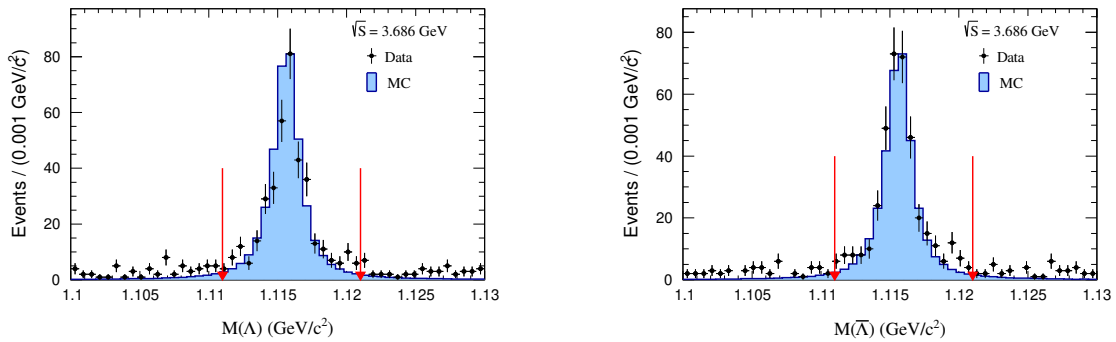


Fig. 2: The distributions of $M(p\pi^-)$ (left) and $M(\bar{p}\pi^+)$ (right). Dots with error bars represent data, the blue histograms are the normalized signal MC. The mass window requirement of the $\Lambda(\bar{\Lambda})$ is shown with the red arrows.

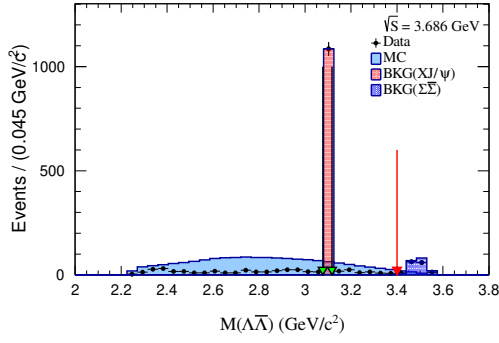


Fig. 3: The distribution of $M(\Lambda\bar{\Lambda})$. The green arrows indicate the veto region for J/ψ background events while the red arrows indicate the veto region for $\psi(3686) \rightarrow \Sigma^0\bar{\Sigma}^0$ events.

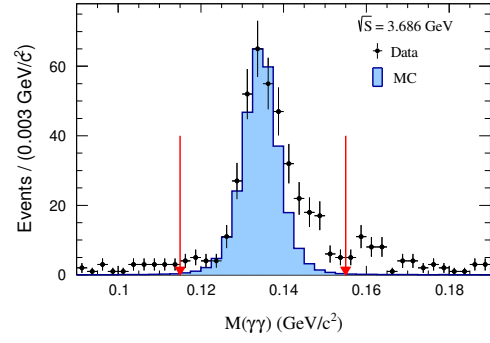


Fig. 4: The distribution of $M(\gamma\gamma)$. Dots with error bars represent data, the blue histograms are normalized signal MC. The signal region is shown with the red arrows.

- The peaking background event from the $\psi(3686) \rightarrow X + J/\psi$ and $\psi(3686) \rightarrow \Sigma^0\bar{\Sigma}^0$ are rejected with the criteria $M(\Lambda\bar{\Lambda}) \notin (3.077, 3.117) \text{ GeV}/c^2$ and $M(\Lambda\bar{\Lambda}) < 3.4 \text{ GeV}/c^2$ as shown in Fig. 3.
- To select π^0 signals, $M(\gamma\gamma)$ is required to be within $[0.115, 0.155] \text{ GeV}/c^2$ mass window, as shown in Fig. 4.
- In order to suppress possible background events from $\psi(3686) \rightarrow \pi^+\pi^- J/\psi$, $J/\psi \rightarrow p\bar{p}\pi^0$, the recoiling mass against the $\pi^+\pi^-$, $M_{\text{rec}}(\pi^+\pi^-)$ as shown in Fig. 5, is required to satisfied $M_{\text{rec}}(\pi^+\pi^-) < 3.087 \text{ GeV}/c^2$ and $M_{\text{rec}}(\pi^+\pi^-) > 3.107 \text{ GeV}/c^2$.

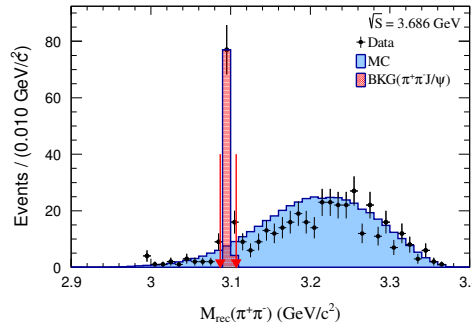


Fig. 5: The distribution of $M_{\text{rec}}(\pi^+\pi^-)$ and red color histograms represent the backgrounds.

- The invariant mass of $M(\gamma_{\text{lower}}\Lambda)$ and $M(\gamma_{\text{lower}}\bar{\Lambda})$ are both required to be outside of the range $(1.183, 1.203) \text{ GeV}/c^2$ to suppress the background from $\psi(3686) \rightarrow \Lambda\bar{\Lambda}\pi^0$, where γ_{lower} represents the energetic photon, as shown in Fig. 6.

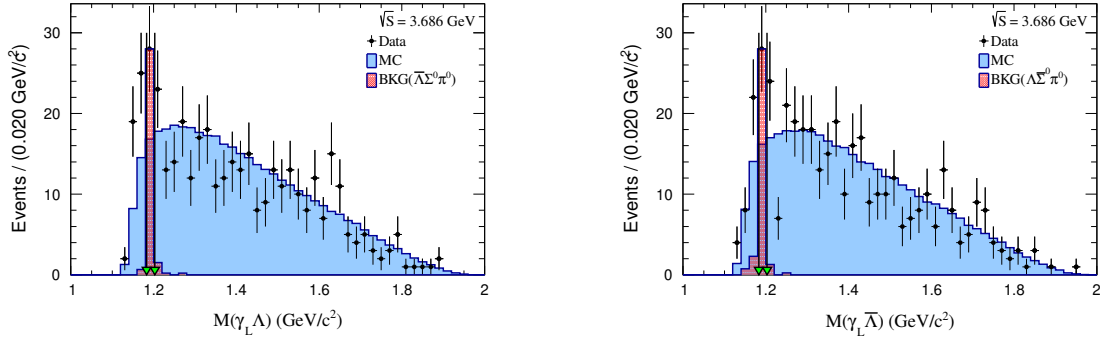


Fig. 6: The distributions of $M(\gamma_{\text{low}}\Lambda)$ (left) and $M(\gamma_{\text{low}}\bar{\Lambda})$ (right). Dots with error bars represent data; the blue histograms are normalized signal MC. The mass window requirement is shown with the green arrows.

- The invariant mass of $M(p\pi^0/\bar{p}\pi^0) < 1.17 \text{ GeV}/c^2$ and $M(p\pi^0/\bar{p}\pi^0) > 1.20 \text{ GeV}/c^2$, are applied to suppress background from $\psi(3686) \rightarrow \Lambda\bar{\Sigma}^-\pi^+ + c.c.$, as shown in Fig. 7.

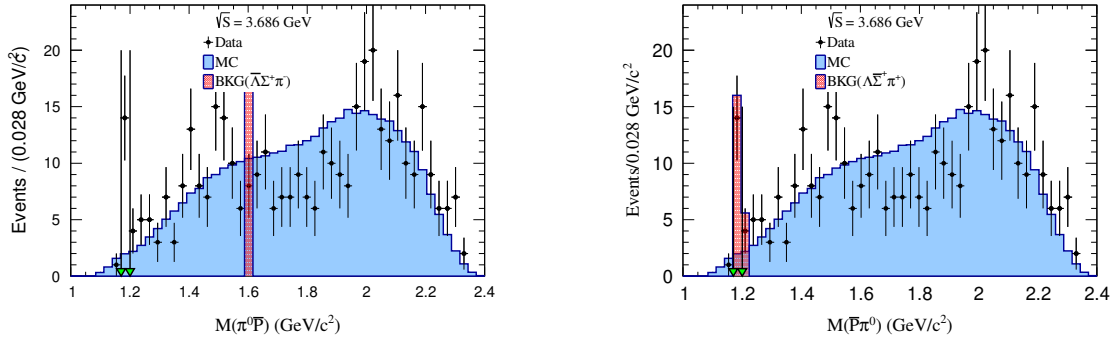


Fig. 7: The distributions of $M(p\pi^0)$ (left) and $M(\bar{p}\pi^0)$ (right). Dots with error bars represent data, the blue histograms are normalized signal MC. The mass window requirement is shown with the green arrows.

- Other 4C-kinematic fits of the $\psi(3686) \rightarrow \Lambda\bar{\Lambda}\gamma$ and $\psi(3686) \rightarrow \Lambda\bar{\Lambda}\gamma\gamma\gamma$ hypotheses are also performed and their corresponding $\chi_{4C}^2(\gamma)$ and $\chi_{4C}^2(3\gamma)$ are required to be larger than $\chi_{4C}^2(2\gamma)$. Table 2 listed the cut flow of each condition.

5.2 Background estimation

The same study of 2.7 billion $\psi(3686)$ inclusive MC sample is performed to investigate possible background event for $\psi(3686) \rightarrow \Lambda\bar{\Lambda}\pi^0$. The surviving background events are listed in Table 17 by topologic analysis using TopoAna package [31]. From the topology analysis and the previous work [32],

Selection criteria	Number of surviving events	Absolute ratio of surviving events (%)	Relative ratio over the last criterion (%)
Total	2.7×10^6	100%	100%
Good charged track	1510086	55.92	55.92
Good photon	1387869	51.40	91.90
Reconstruction of $\Lambda(\bar{\Lambda})$	1253676	46.43	96.09
4C kinematic fit	829198	30.71	66.14
$M(\gamma\gamma) \in (0.525, 0.560) \text{ GeV}/c^2$	714420	26.46	86.16
$M(p\pi^-) \in (1.111, 1.121) \text{ GeV}/c^2$	613440	22.72	85.84
$M(\bar{p}\pi^+) \in (1.111, 1.121) \text{ GeV}/c^2$	528120	19.56	86.11
$\chi_{4C}^2 < 15$	394740	14.62	74.72
$M(\Lambda\bar{\Lambda}) < 3.4 \text{ GeV}/c^2$	379080	14.04	96.09
$M(\Lambda\bar{\Lambda}) \notin (3.077, 3.117) \text{ GeV}/c^2$	365400	13.50	96.10
$M_{\text{rec}}(\pi^+\pi^-) \notin (3.087, 3.107) \text{ GeV}/c^2$	350460	12.98	96.19
$\chi_{4C}^2(2\gamma) < \chi_{4C}^2(3\gamma)$	346140	12.82	98.75
$\chi_{4C}^2(2\gamma) < \chi_{4C}^2(1\gamma)$	345870	12.81	99.86
$M(\gamma_L\Lambda) \notin (1.183, 1.203) \text{ GeV}/c^2$	329670	12.21	95.32
$M(\gamma_L\Lambda/\gamma_L\bar{\Lambda}) \notin (1.183, 1.203) \text{ GeV}/c^2$	315360	11.68	95.67
$M(p\pi^0\Lambda/\bar{p}\pi^0) \notin (1.17, 1.2) \text{ GeV}/c^2$	311310	11.53	99.53

Tab. 2: Cut flow of $\psi(3686) \rightarrow \Lambda\bar{\Lambda}\pi^0$.

it is found that the main background events come from $\psi(3686) \rightarrow \Lambda\bar{\Sigma}^0\pi^0 + c.c.$, which contribute to a peak background.

5.2.1 Hadronic background

A dedicated MC sample of 10 million $\psi(3686) \rightarrow \Lambda\bar{\Sigma}^0\pi^0 + c.c.$ is generated and is analyzed to estimate its detection efficiency, according to its simulation detector efficiency and branching fraction of PDG [27]. The number of the normalization background event is determined to 120 ± 1 .

5.2.2 QED continuum background

The background contribution from QED continuous processes is studied. We perform a study with the sample of 20,274.8 pb⁻¹ at $\sqrt{s} = 3.773$ GeV. After the same event selection as described above, a clear π^0 peak is seen. To obtain the number of π^0 events by fitting $M(\gamma\gamma)$, the MC shape of the π^0 convolved with a Gaussian function is used to describe the signal shape. The fitting result of $M(\gamma\gamma)$ is shown in Fig. 8, and π^0 events from the QED continuum background are determined to be 608 ± 25 . The normalization factor is determined as this formula

$$f_c = \frac{N_{obs}^{3686}}{N_{obs}^{3773}} = \frac{\mathcal{L}^{3686} \times \sigma^{Borm}(3.686) \times \epsilon^{3686}}{\mathcal{L}^{3773} \times \sigma^{Borm}(3.773) \times \epsilon^{3773}} \quad (1)$$

where $N, \mathcal{L}, \sigma, \epsilon$ are the observed number events, integrated luminosity of data samples, cross section, and detection efficiency at the two c.m. energies, respectively. All these corresponding values are listed in Table 3. The scale factor is estimated to be 0.178 and residual continuum background is determined to be 108 ± 4 .

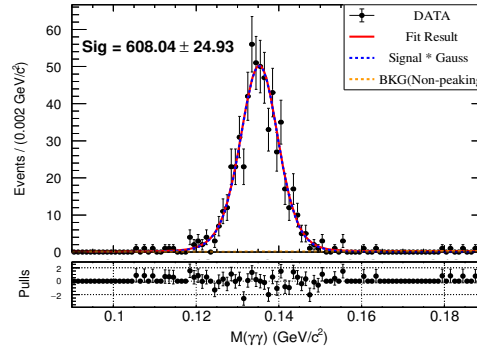


Fig. 8: The fit to $M(\gamma\gamma)$. Dots with error bars are data, red solid curves are fitting results, blue dashed curve is the signal MC shape, orange dashed line is the flat background.

Source	Value
$\mathcal{L}_{\psi(3686)} / \mathcal{L}_{\psi(3770)}$	0.191
$\sigma_{\psi(3686)} / \sigma_{\psi(3770)}$	1.047
$\epsilon_{\psi(3686)} / \epsilon_{\psi(3770)}$	0.889

Tab. 3: Relative values for $\psi(3686)$ and $\psi(3770)$.

5.3 Mass Spectrum Fitting

An extended unbinned maximum likelihood fit is performed on the $M(\gamma\gamma)$ distribution as presented in Fig. 9. In this fit, the π^0 signal is modeled with a signal Monte Carlo (MC) shape convoluted with a single Gaussian function. The non-peaking background is parameterized by a first-order Chebyshev polynomial function. Additionally, the QED continuum background is derived from the shape obtained from continuum data collected at $\sqrt{S} = 3.773$ GeV and its number is fixed to 108 ± 4 . The peaking background is described by the MC shape and its number is fixed to 120 ± 1 . The fit, as illustrated in Fig. 9, yields $N_{\pi^0}^{obs} = 119 \pm 20$ π^0 signal events.

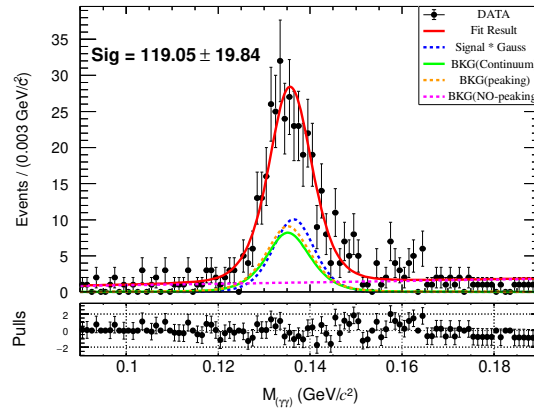


Fig. 9: The fit to $M(\gamma\gamma)$. Dots with error bars are data, red solid curves is the fit result, blue dashed line is the MC signal, pink curve is the non-peaking background, orange curve shows the $\psi(3686) \rightarrow \Lambda \bar{\Sigma}^0 \pi^0 + c.c.$, green curve is the continuum background.

5.4 Branching Fraction Calculation

The branching fraction $\mathcal{B}(\psi(3686) \rightarrow \Lambda \bar{\Lambda} \pi^0)$ is calculated with

$$\begin{aligned} \mathcal{B}(\psi(3686) \rightarrow \Lambda \bar{\Lambda} \pi^0) &= \frac{N_{\pi^0}^{obs}}{N_{\psi(3686)} \cdot \mathcal{B}^2(\Lambda \rightarrow p \pi^-) \cdot \mathcal{B}(\pi^0 \rightarrow \gamma\gamma) \cdot \epsilon} \\ &= (0.93 \pm 0.15) \times 10^{-6}. \end{aligned}$$

where, $N_{\psi(3686)} = (2712.4 \pm 14.3) \times 10^6$ represents the number of $\psi(3686)$ events [19], while $\epsilon = 11.62\%$ is the detection efficiency from Monte Carlo simulation with a uniform distribution. The decay branching fractions $\mathcal{B}(\Lambda \rightarrow p \pi^-)$ and $\mathcal{B}(\pi^0 \rightarrow \gamma\gamma)$ are taken from the Particle Data Group (PDG) [27]. Here the uncertainty is statistical only.

6 Partial wave analysis of $\psi(3686) \rightarrow \Lambda \bar{\Lambda} \eta$

6.1 Final Event Selection

- The χ_{4C}^2 distribution between data and MC is shown in Fig. 10, and is further required to be less than 40.

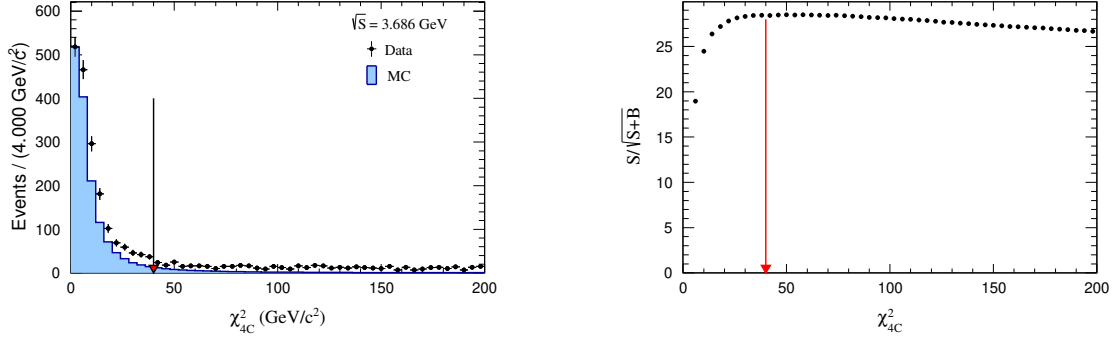


Fig. 10: The distributions of χ_{4C}^2 distribution (left) and optimization of χ_{4C}^2 (right). The dots represent the data sample while the histogram with a blue solid line represents the signal MC sample, which has been normalized to match the data sample.

- In order to suppress the influence of backgrounds on the signal events and improve signal purity, the $M(p\pi^-)$ and the $M(\bar{p}\pi^+)$ are required to be within this mass region $[1.111, 1.121] \text{ GeV}/c^2$, as shown in Fig. 11.

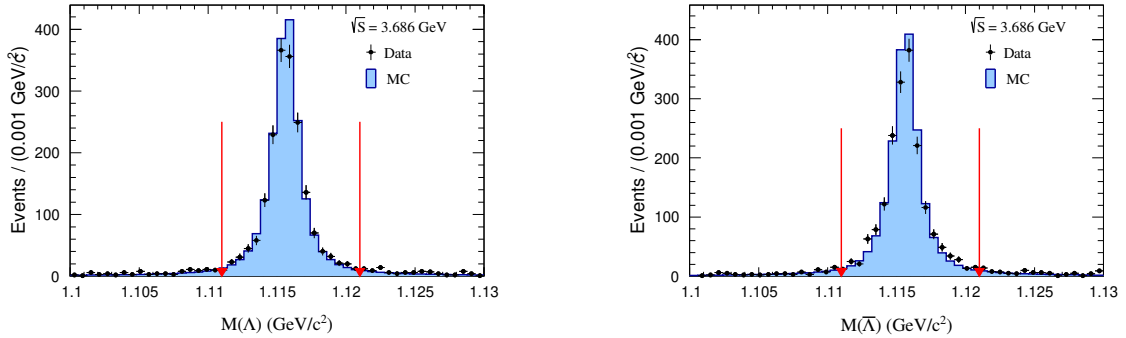


Fig. 11: The distributions of $M(p\pi^-)$ (left) and $M(\bar{p}\pi^+)$ (right). Dots with error bars represent data; the blue histograms are the normalized signal MC. The mass window requirement of the $\Lambda(\bar{\Lambda})$ is shown with the red arrows.

- In order to suppress the influence of backgrounds on the signal events and improve signal purity, the η candidate is selected with the requirement of $M(\gamma\gamma)$ within $[0.525, 0.560] \text{ GeV}/c^2$, as shown

in Fig. 12.

- To reject peaking background from the $\psi(3686) \rightarrow X + J/\psi$, we require the invariant mass $M(\Lambda\bar{\Lambda})$ to be less than $3.077 \text{ GeV}/c^2$, as shown in Fig. 13.

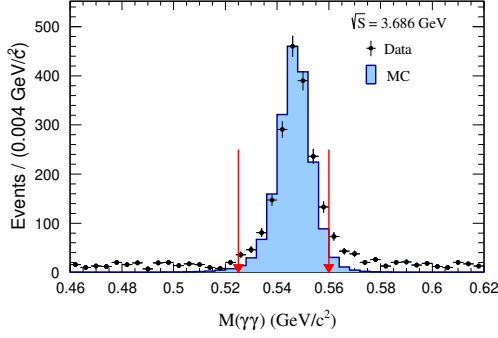


Fig. 12: The distribution of $M(\gamma\gamma)$. Dots with error bars represent data, the blue histograms are normalized signal MC. The mass window requirement is shown with the red arrows.

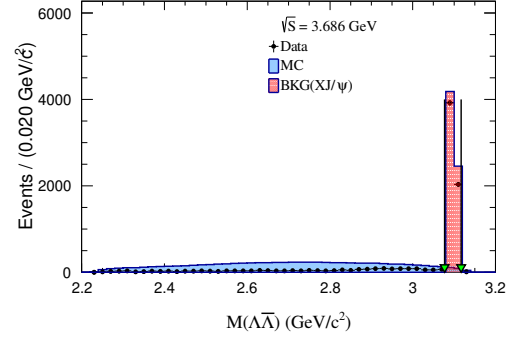


Fig. 13: The distribution of $M(\Lambda\bar{\Lambda})$. The green arrows indicate the veto region for J/ψ events, dots with error bars represent data, and the blue histograms are normalized signal MC.

- To remove possible background events from $\psi(3686) \rightarrow \pi^+\pi^- J/\psi$, $J/\psi \rightarrow p\bar{p}\eta$, the mass recoiling against the $\pi^+\pi^-$ is required to satisfy $M_{\text{rec}(\pi^+\pi^-)} < 3.087 \text{ GeV}/c^2$ and $M_{\text{rec}(\pi^+\pi^-)} > 3.107 \text{ GeV}/c^2$, as shown in Fig. 14.

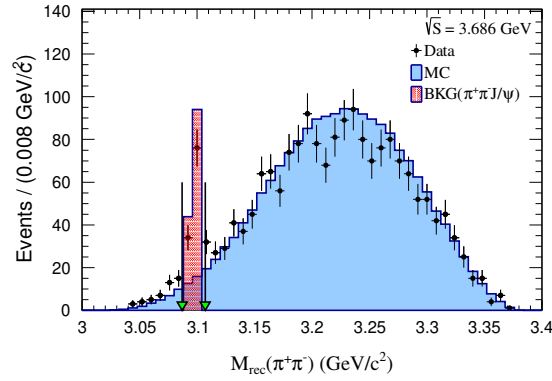


Fig. 14: The distribution of $M_{\text{rec}(\pi^+\pi^-)}$ and red color histograms represent the backgrounds.

- To further suppress other non-peaking background, the χ^2 of the 4C kinematic fit of the $\psi(3686) \rightarrow \Lambda\bar{\Lambda}\gamma\gamma$ hypothesis is performed, and $\chi^2_{4C}(3\gamma)$ is required to be larger than $\chi^2_{4C}(2\gamma)$. The cut flow of the selection is shown in Table 4.

Selection criteria	Number of surviving events	Absolute ratio of surviving events (%)	Relative ratio over the last criterion(%)
Total	2.7×10^6	100%	100%
Good charged track	1447333	53.60	53.60
Good photon	1372585	50.83	94.83
Reconstruction of $\Lambda(\bar{\Lambda})$	1220309	45.19	88.90
4C kinematic fit	732727	27.13	60.04
$M(\gamma\gamma) \in (0.525, 0.560) \text{ GeV}/c^2$	555390	20.57	75.82
$M(p\pi^-) \in (1.111, 1.121) \text{ GeV}/c^2$	496800	18.40	89.41
$M(\bar{p}\pi^+) \in (1.111, 1.121) \text{ GeV}/c^2$	445770	16.51	89.72
$\chi_{4C}^2 < 40$	11111	417960	93.78
$M(\Lambda\bar{\Lambda}) < 3.077 \text{ GeV}/c^2$	402840	14.92	96.37
$\chi_{4C}^2(2\gamma) < \chi_{4C}^2(3\gamma)$	400140	14.82	91%
$M_{rec}(\pi^+\pi^-) \notin (3.087, 3.107) \text{ GeV}/c^2$	395010	14.63	98.10

Tab. 4: Cut flow of $\psi(3686) \rightarrow \Lambda\bar{\Lambda}\eta$.

6.2 Background estimation

The same study of 2.7 billion $\psi(3686)$ inclusive MC sample is performed to investigate possible background event for $\psi(3686) \rightarrow \Lambda\bar{\Lambda}\eta$. The surviving background events are listed in Table 18 by topological analysis using TopoAna package [31]. From the topology analysis, it is found that the background events have no peaking background under the η peak.

The background contribution from QED continuous processes is studied. We perform a study with the sample of $20,274.8 \text{ pb}^{-1}$ at $\sqrt{s} = 3.773 \text{ GeV}$. After the same event selection as described above, a clear η peak is seen. These background events are estimated by fitting the $M(\gamma\gamma)$ as shown in Fig. 15 and determined to be 705.4 ± 27.5 . The Born cross section of $e^+e^- \rightarrow \Lambda\bar{\Lambda}\eta$ has been well studied [12]. The normalization factor is determined as this formula

$$f_c = \frac{N_{obs}^{3686}}{N_{obs}^{3773}} = \frac{\mathcal{L}^{3686} \times \sigma^{Born}(3.686) \times \epsilon^{3686}}{\mathcal{L}^{3773} \times \sigma^{Born}(3.773) \times \epsilon^{3773}}$$

where $N, \mathcal{L}, \sigma, \epsilon$ are the observed number events, integrated luminosity of data samples, cross section, and detection efficiency at the two c.m. energies, respectively. The result is in Table 5. The scale factor is estimated to be 0.181 and the residual continuum background is determined to be 128.3 ± 5.0 .

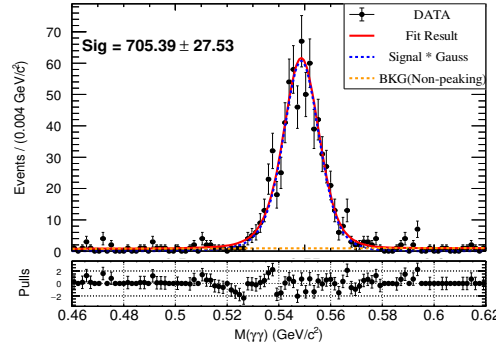


Fig. 15: The fit to $M(\gamma\gamma)$. Dots with error bars are data, red solid curves are fitting results, blue dashed curve is the signal MC shape, orange dashed line is the flat background.

Source	Value
$\mathcal{L}_{\psi(3686)}/\mathcal{L}_{\psi(3770)}$	0.191
$\sigma_{\psi(3686)}/\sigma_{\psi(3770)}$	1.047
$\epsilon_{\psi(3686)}/\epsilon_{\psi(3770)}$	0.907

Tab. 5: Relative values for $\psi(3686)$ and $\psi(3770)$.

261 6.3 Mass Spectrum Fitting

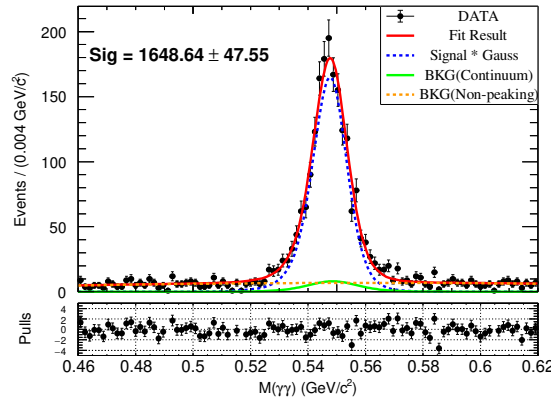


Fig. 16: The fit to $M(\gamma\gamma)$. Dots with error bars are data, red solid curves is the result, blue dashed line is the signal, orange curve is the non-peaking background, green curve is the continuum background.

262 To determine the signal yield, an extended unbinned maximum likelihood fit is performed on the
 263 $M(\gamma\gamma)$ distribution, as shown in Fig. 16. In this fit, the η signal is modeled with a signal Monte Carlo
 264 shape convoluted with a single Gaussian function. The non-peaking background is parameterized by a

first-order Chebyshev polynomial function. Additionally, the continuum background shape is derived from the shape obtained from continuum data collected at $\sqrt{s} = 3.773$ GeV and its number is fixed to 128.3 ± 5.0 . The fitting result is illustrated in Fig. 16, and the number of η signal events is determined to be 1648.6 ± 47.6 .

6.4 Partial wave analysis

6.4.1 Data Distribution

After the above event selection, 1816 events survived. Figure 17 shows the $m_{\Lambda\eta}$, $m_{\bar{\Lambda}\eta}$, and $m_{\Lambda\bar{\Lambda}}$ mass spectra of $\psi(3686)$. Here, non-peak background from η sideband and continuum background are also shown in Fig. 17. A significant $\Lambda(1670)$ signal is observed in the $m_{\Lambda\eta}$ around mass threshold of $\Lambda\eta$ system.

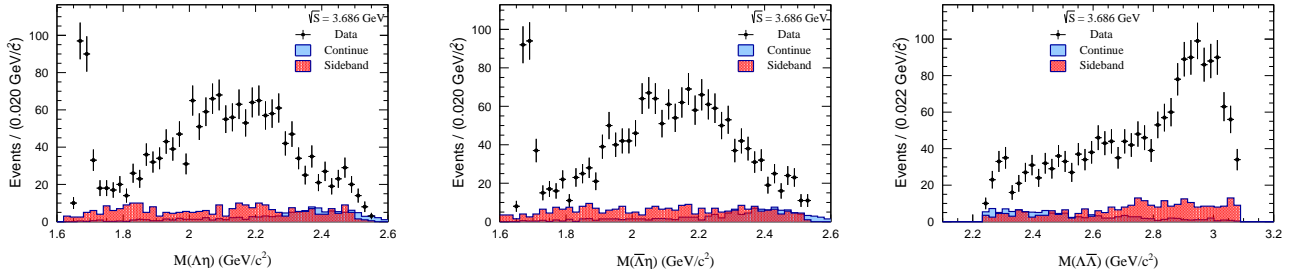


Fig. 17: Distributions of $m_{\Lambda\eta}$ (left), $m_{\bar{\Lambda}\eta}$ (middle), and $m_{\Lambda\bar{\Lambda}}$ (right). The dots with error bars are from $\psi(3686)$ data sample. The red hatched histogram is non-peak background from η sideband and the blue shadow comes is for the continue background.

6.4.2 Background Treatment

The non- η background events are estimated from the η -sideband regions of $0.470 \text{ GeV}/c^2 < M(\gamma\gamma) < 0.505 \text{ GeV}/c^2$ and $0.580 \text{ GeV}/c^2 < M(\gamma\gamma) < 0.615 \text{ GeV}/c^2$, which are indicated in Fig. 18.

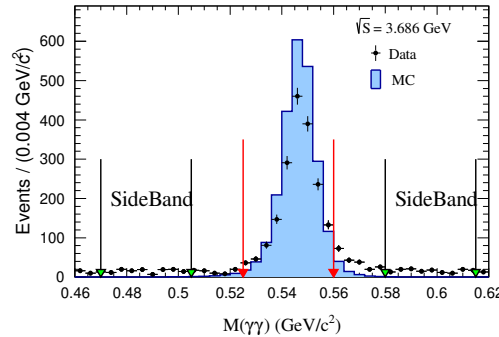


Fig. 18: Definition of the η signal and sideband regions.

6.5 PWA method

We use the TensorFlow Partial Wave Analysis(TFPWA) package [33] is performed in this analysis. The full decay amplitude of the decay $\psi(3686) \rightarrow \Lambda \bar{\Lambda} \eta$ is constructed with the helicity formalism based on the Isobar model describing the three-body decay as a two-step sequential quasi-two-body decay. For each two-body decay $0 \rightarrow 1 + 2$ the helicity amplitude can be written as

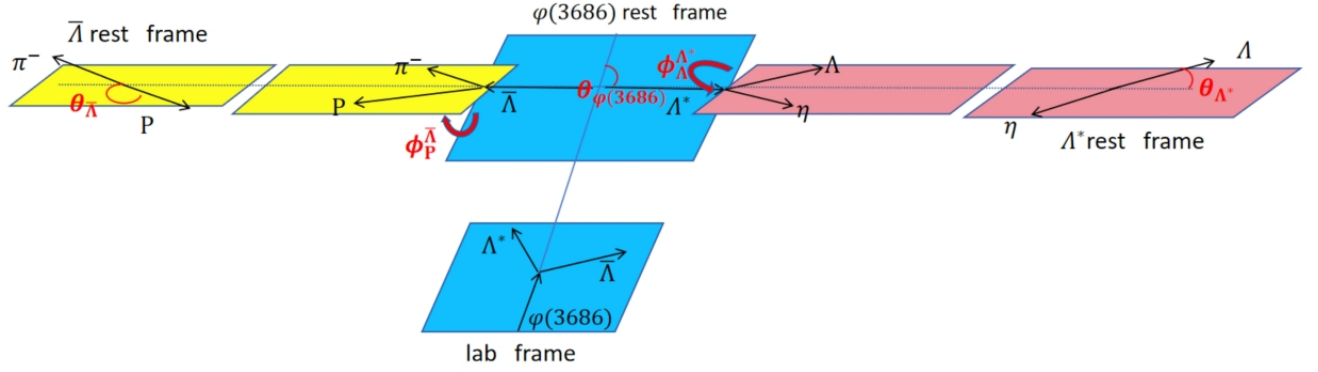


Fig. 19: Definitions for the helicity angles with decay chains

$$A_{\lambda_0, \lambda_1, \lambda_2}^{0 \rightarrow 1+2} = H_{\lambda_1, \lambda_2}^{0 \rightarrow 1+2} D_{\lambda_0, \lambda_1 - \lambda_2}^{J_0*}(\phi, \theta, 0) \quad (2)$$

where the amplitude $H_{\lambda_1, \lambda_2}^{0 \rightarrow 1+2}$ is given by the LS coupling formula [34] along with baryon factor terms

$$H_{\lambda_1, \lambda_2}^{0 \rightarrow 1+2} = \sum_{ls} g_{ls} \sqrt{\frac{2l+1}{2J_0+1}} \langle l0, s\delta | J_0, \delta \rangle \langle J_1 J_2, \lambda_1 - \lambda_2 | s, \delta \rangle \left(\frac{q}{q_0} \right)^l B'_l(q, q_0, d), \quad (3)$$

where g_{ls} is the partial wave amplitude, J_0, J_1, J_2 are the spin of the particles 0, 1, and 2. λ_1, λ_2 are the helicities for particles 1 and 2, and $\delta = \lambda_1 - \lambda_2$ is the helicity difference. Here, q is the three-momentum modulus of particle 1 in the rest frame of particle 0, which is calculated as

$$q = \frac{\sqrt{[m^2 - (m_1 + m_2)^2][m^2 - (m_1 - m_2)^2]}}{2m} \quad (4)$$

where m, m_1 , and m_2 are the masses of the particles 0, 1, and 2, respectively. The normalization factor q_0 is calculated at the nominal resonance mass. The factor $B'_l(q, q_0, d)$ is the reduced Blatt-Weisskopf

289 barrier factor [35], which is explicitly expressed as

$$\begin{aligned}
 B'_0(q, q_0, d) &= 1, \\
 B'_1(q, q_0, d) &= \sqrt{\frac{1 + (q_0 d)^2}{1 + (q d)^2}}, \\
 B'_2(q, q_0, d) &= \sqrt{\frac{9 + 3(q_0 d)^2 + (q_0 d)^4}{9 + 3(q d)^2 + (q d)^4}}, \\
 B'_3(q, q_0, d) &= \sqrt{\frac{225 + 45(q_0 d)^2 + 6(q_0 d)^4 + (q_0 d)^6}{225 + 45(q d)^2 + 6(q d)^4 + (q d)^6}}, \\
 B'_4(q, q_0, d) &= \sqrt{\frac{11025 + 1575(q_0 d)^2 + 135(q_0 d)^4 + 10(q_0 d)^6 + (q_0 d)^8}{11025 + 1575(q d)^2 + 135(q d)^4 + 10(q d)^6 + (q d)^8}}.
 \end{aligned} \tag{5}$$

290 In the Wigner D -function, $D_{\lambda_0, \lambda_1 - \lambda_2}^{J_0^*}(\phi, \theta, 0)$, ϕ and θ are helicity angles, and are shown in Fig. 19.
 291 The definitions can be found in ref. [36]. In eq. (6), the radius d is chosen as $d = 0.73$ fm, which is
 292 the same as in ref. [37]. The amplitude for a complete decay chain is constructed as the product of each
 293 two-body decay amplitude and the resonant propagator R . For example, in the sequential decay

$$\psi(3686) \rightarrow \Lambda^* \bar{\Lambda}, \quad \Lambda^* \rightarrow \Lambda \eta, \quad \bar{\Lambda} \rightarrow \bar{p} \pi^+,$$

294 the amplitude is written as

$$A_{\lambda_{\psi(3686)}, \lambda_{\Lambda^*}}^{\Lambda^*} = \sum_{\lambda_{\Lambda^*}, \lambda_{\Lambda}} A_{\lambda_{\psi(3686)}, \lambda_{\Lambda^*}, \lambda_{\Lambda}}^{\psi(3686) \rightarrow \Lambda^* \Lambda} R_{\Lambda^*}(M_{\Lambda \eta}) A_{\lambda_{\Lambda^*}, 0, 0}^{\Lambda^* \rightarrow \Lambda \eta} A_{\lambda_{\Lambda}, \lambda_p, 0}^{\Lambda \rightarrow p \pi^-}. \tag{6}$$

295 For the non-resonant (NR) decay, the amplitude A_{λ}^{NR} is replaced by setting $R_{NR}(M_{\Lambda \eta})$ as unity, ex-
 296 pressed as

$$A_{\lambda_{\Lambda^*}, \lambda_p}^{NR} = \sum_{\lambda_{NR}, \lambda_{\Lambda}} A_{\lambda_{\Lambda^*}, \lambda_{NR}, \lambda_{\Lambda}}^{\Lambda^* \rightarrow NR + \Lambda} A_{\lambda_{NR}, 0, 0}^{NR \rightarrow \pi^+ \pi^0} A_{\lambda_{\Lambda}, \lambda_p, 0}^{\Lambda \rightarrow p \pi^-}. \tag{7}$$

297 The relativistic Breit-Wigner formula for the $\Lambda(1800)$ resonance is given by:

$$R_{\Lambda(1800)}(m) = \frac{1}{m_0^2 - m^2 - i m_0 \Gamma(m)} \tag{8}$$

298 The mass-dependent width is defined as:

$$\Gamma(m) = \Gamma_0 \left(\frac{q}{q_0} \right)^{2l+1} \frac{m_0}{m} B_l'^2(q, q_0, d) \tag{9}$$

299 For the $\Lambda(1670)$ resonance, the decay channel's threshold is positioned **below** the nominal resonance
 300 mass. Therefore the Flatté-model is used

$$R(m) = \frac{1}{m_0^2 - m^2 - im_0 \left[\sum_i g_i \frac{q_i}{m} \times \frac{m_0}{|q_i|} \times \frac{|q_i|^{l_i}}{|q_{i0}|^{2l_i}} B_{l_i}'^2(|q_i|, |q_{i0}|, d) \right]} \quad (10)$$

$$q_i = \begin{cases} \frac{\sqrt{(m^2 - (m_{i,1} + m_{i,2})^2)(m^2 - (m_{i,1} - m_{i,2})^2)}}{2m} & \text{if } (m^2 - (m_{i,1} + m_{i,2})^2)(m^2 - (m_{i,1} - m_{i,2})^2) \geq 0 \\ i \frac{\sqrt{|(m^2 - (m_{i,1} + m_{i,2})^2)(m^2 - (m_{i,1} - m_{i,2})^2)|}}{2m} & \text{if } (m^2 - (m_{i,1} + m_{i,2})^2)(m^2 - (m_{i,1} - m_{i,2})^2) < 0 \end{cases} \quad (11)$$

301 The coupling g_i constants are represented by $g_i \propto M(1670) \cdot \sum_i \text{BR}_i$. Here $i(= 0, 1, \dots)$ runs over all
 302 decay channels of the $\Lambda(1670)$ resonance, including $\bar{K}N \rightarrow \Lambda(1670) \rightarrow \bar{K}N$, $\Sigma\pi$, and $\Lambda\eta$. BR_j is the
 303 branching ratio for the corresponding process.

304 6.6 Likelihood function construction and fit fraction

305 The probability density function for a given event constructed using the full amplitude as

$$P = \frac{|\mathcal{A}|^2}{\int |\mathcal{A}|^2 d\Phi}, \quad |\mathcal{A}|^2 = \frac{1}{2} \sum_{\lambda_{\psi(3686)}, \lambda_{\Lambda}^*} |\mathcal{A}_{\lambda_{\psi(3686)}, \lambda_{\Lambda}^*}|^2. \quad (12)$$

306 where the factor $\frac{1}{2}$ arises from the average of the initial $\psi(3686)$ spin under the assumption of ho-
 307 mogeneously polarization. Possible polarization effects are considered with the systematic uncertainties.
 308 The integration is calculated with a large MC PHSP sample passing the simulated detector reconstruction
 309 stage, and we have

$$\int |\mathcal{A}|^2 d\Phi \propto \frac{1}{N_{\text{PHSP}}} \sum_{i \in \text{PHSP}} |\mathcal{A}(x_i)|^2. \quad (13)$$

310 The negative log likelihood (NLL) is constructed by summing all signal candidates and subtracting
 311 the η sideband background:

$$-\ln L = -\alpha \left[\sum_{i \in \text{data}} \ln P(x_i) - w'_{\text{bkg}} \sum_{i \in \text{sideband}} \ln P(x_i) \right], \quad (14)$$

312 where $w'_{\text{bkg}} = w_{\text{bkg}} \cdot \frac{N_{\text{data}}}{N_{\text{sideband}}}$, N_{data} and N_{sideband} are the events in the η signal region and sideband
 313 region, respectively. To achieve an unbiased uncertainty estimation, the normalization factor derived
 314 from [38] is taken into account, expressed as

$$\alpha = \frac{N_{\text{data}} - N_{\text{sideband}} w'_{\text{bkg}}}{N_{\text{data}} + N_{\text{sideband}} w_{\text{bkg}}^2}. \quad (15)$$

315 The fit fraction (FF) for each resonant component can be calculated as

$$FF_i = \frac{\int |\mathcal{A}_i|^2 d\Phi'}{\int |\sum_k \mathcal{A}_k|^2 d\Phi'}, \quad (16)$$

where \mathcal{A}_i is the amplitude of the i -th component and the integration is calculated by the sum of truth level PHSP MC samples before requiring detector acceptance. Hence, the FFS of the interference part can be calculated as

$$FF_{i,j} = \frac{\int |\mathcal{A}_i + \mathcal{A}_j|^2 d\Phi'}{\int |\sum_k \mathcal{A}_k|^2 d\Phi'} - FF_i - FF_j. \quad (17)$$

6.7 PWA solution

Table 6 shows the Λ^* states with $J \leq 5/2$ can also decay into $\Lambda\eta$ from PDG [27].

Particle	J^P	MASS (MeV/c ²)	WIDTH (MeV)	Status
$\Lambda(1670)$	$1/2^-$	1674 ± 4	30 ± 5	****
$\Lambda(1690)$	$3/2^-$	1690 ± 10	70 ± 10	****
$\Lambda(1800)$	$1/2^-$	1800 ± 50	200 ± 50	***
$\Lambda(1810)$	$1/2^+$	1790 ± 50	110 ± 60	***
$\Lambda(1820)$	$5/2^+$	1820 ± 5	80 ± 10	****
$\Lambda(1830)$	$5/2^-$	1825 ± 5	90 ± 30	****
$\Lambda(1890)$	$3/2^+$	1890 ± 20	120 ± 40	****
$\Lambda(2000)$	$1/2^-$	2020 ± 16	255 ± 63	*
$\Lambda(2110)$	$5/2^+$	2090 ± 40	250 ± 50	***

Tab. 6: The status of some Λ^* states. A status * * * * means the state is well established and confirmed by several independent analyses.

6.7.1 Baseline solution

Three intermediate states $\Lambda(1670)$, $\Lambda(1800)$, and $\Lambda(2110)$ are included in baseline solution. Their properties are list in Table 6. Due to same the spin number of $\Lambda(1800)$ and $\Lambda(1670)$, those of the mass and width of $\Lambda(1800)$ are fixed to those of PDG. Table 7 shows the mass, width, and quantum number of resonance states involved in baseline solution. The statistical significance of each resonance state is greater than 5σ . Projections of fit result on the mass spectrum $m_{\Lambda\eta}$, $m_{\bar{\Lambda}\eta}$, and $m_{\Lambda\bar{\Lambda}}$ are shown in Fig. 20. Projection of fit result on the helicity angles $\cos\theta_{\Lambda\bar{\Lambda}}$, $\cos\theta_{\Lambda\eta}$, and $\cos\theta_{\bar{\Lambda}\eta}$ are also shown in Fig. 21, respectively. The basic solutions of the partial wave analysis provides a good description of the data and each resonance state interference is smaller as shown in Table 8.

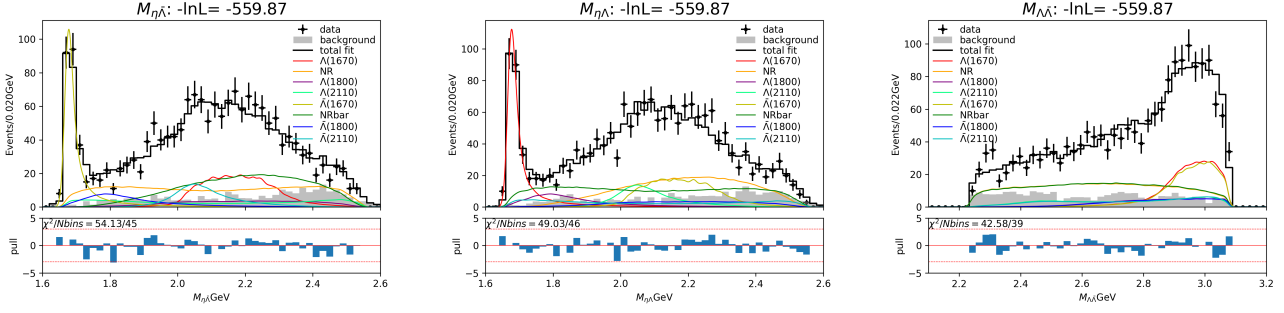


Fig. 20: Projections of fit result of $\psi(3686)$ data sample on $M_{\Lambda\bar{\eta}}$, $M_{\bar{\Lambda}\eta}$, and $M_{\Lambda\bar{\Lambda}}$, from left to right, respectively. The dots with error bars are for data sample. Histograms with various line color show the contribution of each resonance states and their sum.

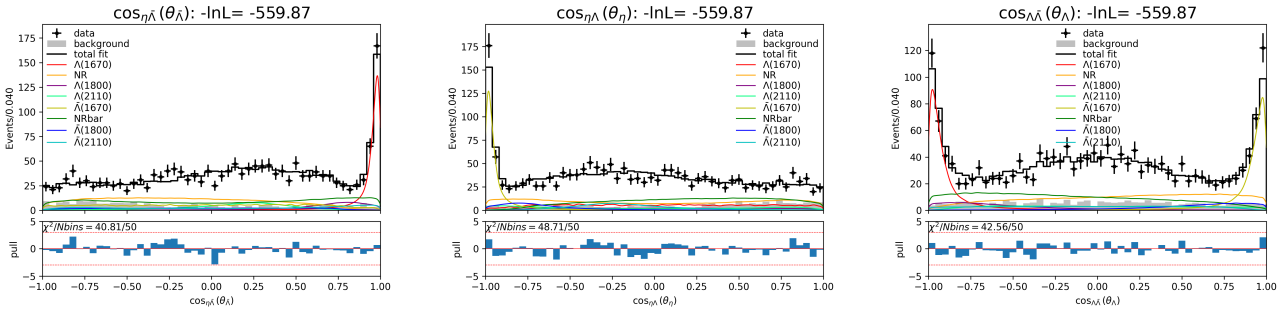


Fig. 21: Projections of fit result of $\psi(3686)$ data sample on three helicity angle $\cos\theta_{\bar{\Lambda}\Lambda}$, $\cos\theta_{\eta\Lambda}$, and $\cos\theta_{\Lambda\bar{\Lambda}}$, from left to right, respectively. The dots with error bars are from $\psi(3686)$ data sample. Histograms with various line color show the contribution of each resonance state and their sum.

Resonance state	Mass (MeV/c ²)	Width (MeV)	$I(J^{PC})$	ΔN_{dof}	Significance (σ)
$\Lambda(1670)$	1674	—	$0(\frac{1}{2}^-)$	5	20.27
$\Lambda(1800)$	1809	220	$0(\frac{1}{2}^-)$	4	5.29
$\Lambda(2110)$	2090	250	$0(\frac{5}{2}^+)$	6	6.23

Tab. 7: Each the resonance state involved in our baseline solution.

Component	<i>Non-resonant</i>	$\Lambda(1670)$	$\Lambda(1800)$	$\Lambda(2110)$
<i>Non-resonant</i>	(41.10 ± 3.55)	-	-	-
$\Lambda(1670)$	(-2.01 ± 1.62)	(37.56 ± 2.43)	-	-
$\Lambda(1800)$	(-8.05 ± 2.13)	(-0.01 ± 0.01)	(13.26 ± 4.75)	-
$\Lambda(2110)$	(-0.01 ± 0.01)	(1.81 ± 1.48)	(-3.42 ± 1.88)	(19.05 ± 1.79)
Total	(110.97 ± 12.5)			

Tab. 8: Fraction of all components and interference between them in unit of percent (%)

6.7.2 IO check

The validation of PWA is performed with 50 toy MC samples generated with the fitted parameters from PWA. The comparison between data sample and toy MC sample are shown in Fig. 22. Figure 23 shows the pull distribution of all Λ^* resonance states.

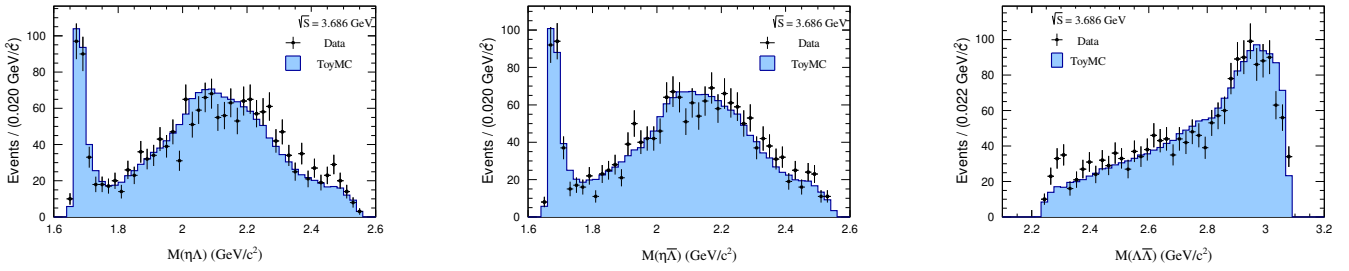


Fig. 22: Comparison between data sample and toy MC samples of $m_{\Lambda\eta}$ (left), $m_{\bar{\Lambda}\eta}$ (middle), and $m_{\Lambda\bar{\Lambda}}$ (right). The dots with error bars are from $\psi(3686)$ data sample. The Histograms with blue area are from toy MC samples.

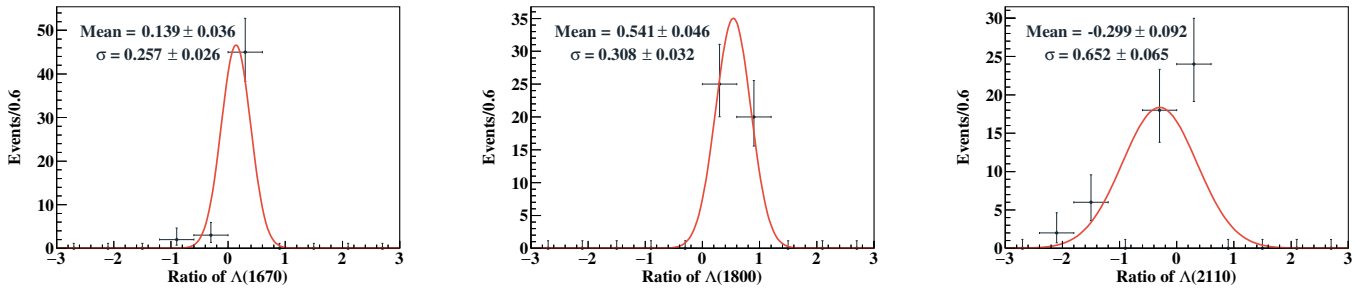


Fig. 23: The pull distributions of fitted fractions of all Λ^* states

6.8 Branching Fraction Calculation

The signal detection efficiency is estimated from a toy MC sample simulation with the fitted parameters of PWA and is obtained to be 15.27%. The branching fraction $\mathcal{B}(\psi(3686) \rightarrow \Lambda \bar{\Lambda} \eta)$ can be calculated as:

$$\begin{aligned} \mathcal{B}(\psi(3686) \rightarrow \Lambda \bar{\Lambda} \eta) &= \frac{N_{\eta}^{\text{obs}}}{N_{\psi(3686)} \cdot \mathcal{B}^2(\Lambda \rightarrow p \pi^-) \cdot \mathcal{B}(\eta \rightarrow \gamma \gamma) \cdot \epsilon} \\ &= (2.43 \pm 0.07) \times 10^{-5}. \end{aligned}$$

Here, N_{η}^{obs} is the net signal yield, ϵ is the efficiency obtained from the toy MC sample, and $N_{\psi(3686)}$ represents the number of $\psi(3686)$ events. The branching fraction of $\psi(3686) \rightarrow \Lambda^* \bar{\Lambda} + c.c.$, ($\Lambda^* \rightarrow \Lambda \eta$) is calculated with the following formula:

$$\mathcal{B}(\psi(3686) \rightarrow \Lambda^* \bar{\Lambda} + c.c.) \times \mathcal{B}(\Lambda^* \rightarrow \Lambda \eta) = \frac{N_{\eta}^{\text{obs}} \times F_{\text{Fraction}}}{N_{\psi(3686)} \cdot \mathcal{B}^2(\Lambda \rightarrow p \pi) \cdot \mathcal{B}(\eta \rightarrow \gamma \gamma) \cdot \epsilon}.$$

Their branching fractions are obtained to be:

$$\mathcal{B}(\psi(3686) \rightarrow \Lambda(1670) \bar{\Lambda}) \times \mathcal{B}(\Lambda(1670) \rightarrow \Lambda \eta) = (0.91 \pm 0.06) \times 10^{-5},$$

$$\mathcal{B}(\psi(3686) \rightarrow \Lambda(1800) \bar{\Lambda}) \times \mathcal{B}(\Lambda(1800) \rightarrow \Lambda \eta) = (0.32 \pm 0.12) \times 10^{-5},$$

$$\mathcal{B}(\psi(3686) \rightarrow \Lambda(2110) \bar{\Lambda}) \times \mathcal{B}(\Lambda(2110) \rightarrow \Lambda \eta) = (0.46 \pm 0.05) \times 10^{-5},$$

respectively.

7 Study of Enhancement near $\Lambda \bar{\Lambda}$ Mass Threshold

7.1 Possible Exotic State

The possible additional exotic state in the $\Lambda \bar{\Lambda}$ mass region from 2.25 GeV/ c^2 to 2.40 GeV/ c^2 is checked in PWA. Within this range, there are no explicitly established resonances of the $\Lambda \bar{\Lambda}$ invariant mass in the PDG [27], with $J^P = 1^{--}$, 2^{--} , and 1^{+-} . The variation of the log-likelihood change with different mass and width values, relative to the baseline solution, is shown in Fig. 24. It is found that the most significant state for the $\Lambda \bar{\Lambda}$ structure has $J^P = 1^{--}$, with a mass of $M = 2291 \pm 5 \text{ MeV}/c^2$, a width of $\Gamma = 25 \pm 8 \text{ MeV}$, and a signal significance of 4.86σ , as listed in Table 9. The fit result projections for $M_{\Lambda \eta}$, $M_{\bar{\Lambda} \eta}$, and $M_{\Lambda \bar{\Lambda}}$ are shown in Fig. 25, along with angular projections in Fig. 26.

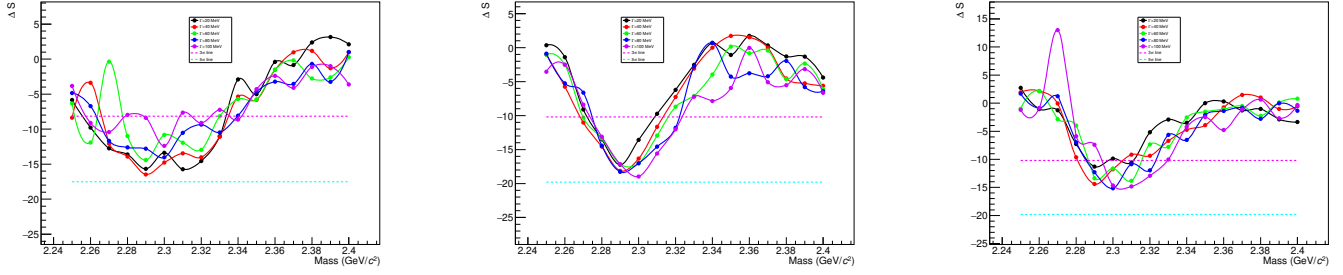


Fig. 24: Additional 1^{--} , 1^{+-} , and 2^{--} states by scanning in the $\Lambda\bar{\Lambda}$ mass, from left to right, respectively. The red dashed line and blue dashed line indicate that the significance of additional state is higher than 3σ and 5σ , respectively.

J^P	Mass (MeV/ c^2)	Width (MeV)	ΔN_{dof}	ΔN_{NLL}	Significance (σ)
1^{--}	2291 ± 5	25 ± 8	6	18.97	4.86
1^{+-}	2300 ± 8	80 ± 1	6	10.97	3.22
2^{--}	2294 ± 5	27 ± 17	8	12.13	3.07

Tab. 9: The fitting results of mass and width for the structure. The errors are statistical only.

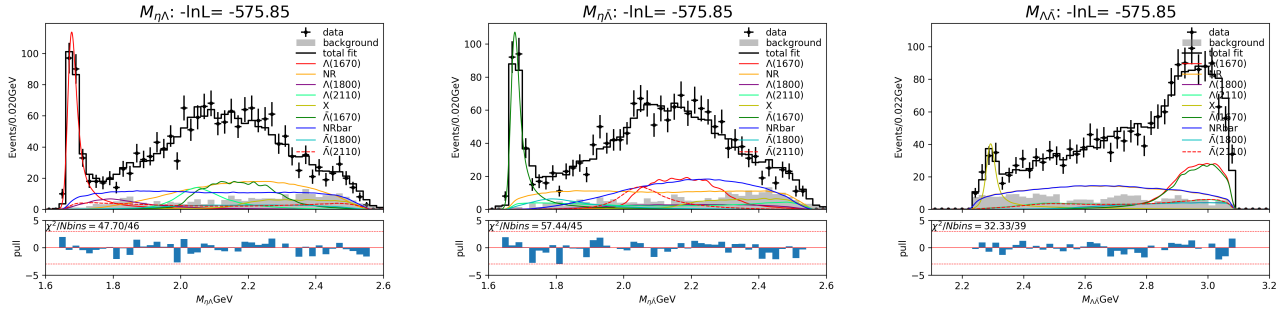


Fig. 25: Projections of fit result of $\psi(3686)$ data sample on $M_{\Lambda\eta}$, $M_{\Lambda\bar{\eta}}$, and $M_{\Lambda\bar{\Lambda}}$, from left to right, respectively. Histograms with various line color show the contribution of each resonance states and their sum.

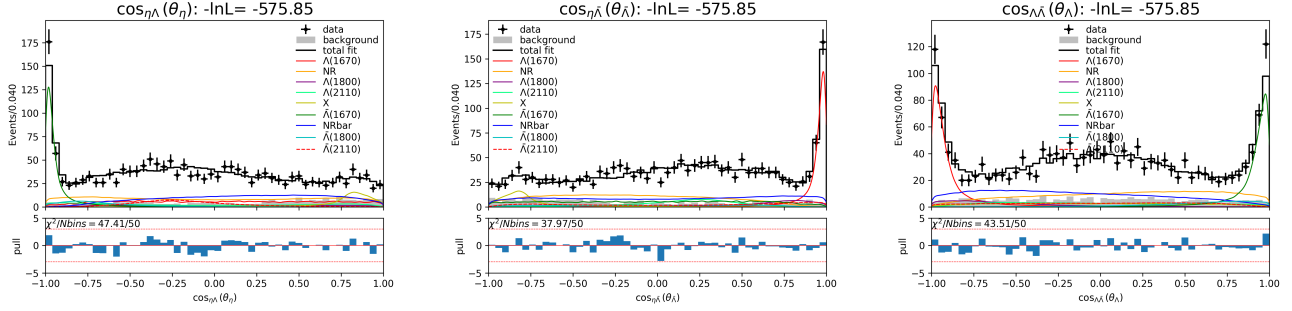


Fig. 26: Projections of fit result of $\psi(3686)$ data sample on three helicity angle $\cos \theta_{\eta\bar{\Lambda}}$, $\cos \theta_{\eta\Lambda}$, and $\cos \theta_{\bar{\Lambda}\Lambda}$, from left to right, respectively.

7.2 Theoretical Models and Experimental Results.

In this analysis, unbinned maximum likelihood fits are performed using the TFPWA package to evaluate the consistency between theoretical models and experimental data.

- A structure was observed through partial wave analysis of PS185 data, with parameters $M = 2290 \pm 20 \text{ MeV}/c^2$ and $\Gamma = 275 \pm 35 \text{ MeV}$ [2].
- A vector hexaquark state is predicted based on the extraction of heading singularities of the amplitude and characterized with a mass of $2100 \text{ MeV}/c^2$ and a width of 33 MeV [9].
- The mass enhancement was observed near the threshold in the process $e^+e^- \rightarrow \eta\Lambda\bar{\Lambda}$ [12] with a mass of $(2356 \pm 7 \pm 15) \text{ MeV}/c^2$ and width of $(304 \pm 28 \pm 54) \text{ MeV}$.
- The near-threshold enhancement was reported in the process $e^+e^- \rightarrow \phi\Lambda\bar{\Lambda}$ [13], whose C parity is 1^{--} and mass and width are $(2262 \pm 4 \pm 28) \text{ MeV}/c^2$ and $(72 \pm 5 \pm 43) \text{ MeV}$, respectively.

The theoretical and experimental results are summarized in the Table 10 below. The statistical significance is calculated based on the change of the NLL values with and without the component, by taking into account the change of the number of degrees of freedom. The current experiments are insufficient to establish the threshold enhancement structure well, with statistical significance less than 3σ .

	Source	J^{PC}	Mass center (MeV/c^2)	Width (MeV)	ΔN_{dof}	ΔN_{NLL}	Significance (σ)
1	Hexaquark state	1^{--}	2100	33	4	5.9	2.3
2	<i>PS 185 data</i>	1^{--}	2290 ± 20	275 ± 35	4	7.4	2.80
3	$e^+e^- \rightarrow \eta\Lambda\bar{\Lambda}$	1^{--}	2356 ± 7	304 ± 28	4	2.0	0.83
4	$e^+e^- \rightarrow \phi\Lambda\bar{\Lambda}$	1^{--}	2262 ± 4	72 ± 5	4	7.6	2.85

Tab. 10: The theoretical and experimental result of the $\Lambda\bar{\Lambda}$ mass threshold.

367

A comprehensive comparison of theoretical predictions and experimental results is shown in Fig. 27.

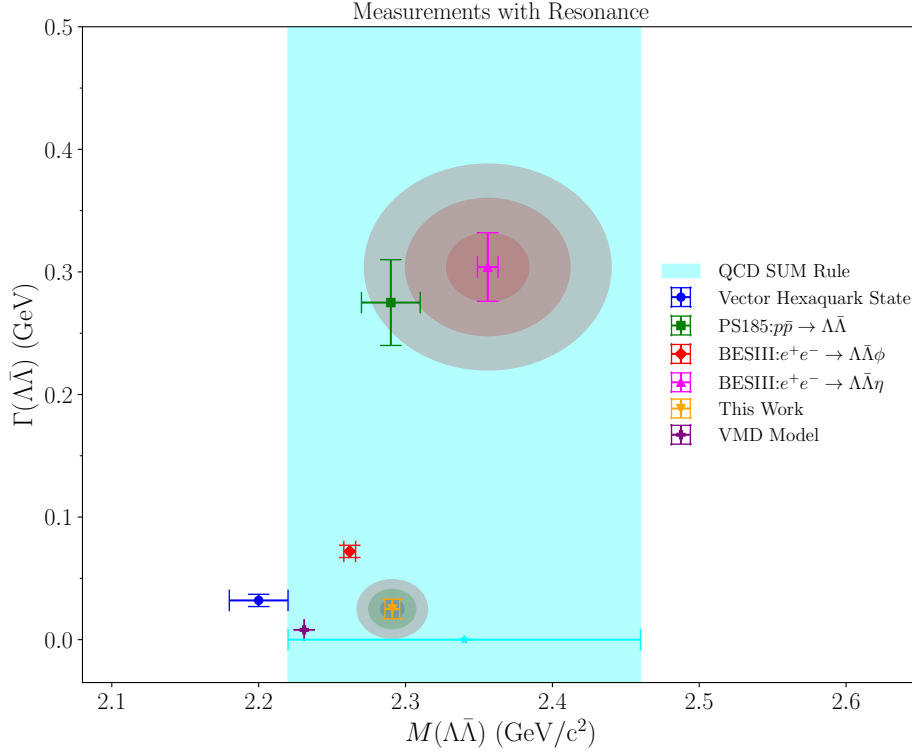


Fig. 27: The blue represents the results from vector hexaquark theory, while red indicates the results from the BESIII collaboration in the process $e^+e^- \rightarrow \phi\Lambda\bar{\Lambda}$. The green corresponds to the partial wave analysis results from the PS185 experiment, and pink denotes the results from the BESIII experiment in the process $e^+e^- \rightarrow \eta\Lambda\bar{\Lambda}$. The cyan color represents QCD theoretical predictions, and the orange and purple colors respectively represent the results from this analysis.

368 8 Systematic Uncertainties

369

There are common systematic uncertainties for the two decays $\psi(3686) \rightarrow \Lambda\bar{\Lambda}\pi^0$ and $\psi(3686) \rightarrow \Lambda\bar{\Lambda}\eta$, which are examined independently.

371

- Number of $\psi(3686)$ events

372

The number of $\psi(3686)$ events is determined to be $(27.12 \pm 0.14) \times 10^8$ [19], and the uncertainty is assigned to be 0.52%.

373

374

- Tracking Efficiency and $\Lambda(\bar{\Lambda})$ Reconstruction

375

The efficiency of $\Lambda(\bar{\Lambda})$ reconstruction is studied using the control sample of $\psi(3686) \rightarrow \Lambda\bar{\Lambda}$ decays, and a correction factor 0.980 ± 0.011 [39] is applied to the efficiencies obtained from MC simulation.

376

377

The uncertainty of the correction factor, 1.1%, already including the uncertainties of MDC tracking efficiency and $\Lambda(\bar{\Lambda})$ second vertex, and 1.1% is taken as the uncertainty of the efficiency of $\Lambda(\bar{\Lambda})$ reconstruction.

378

379

• Photon Detection Efficiency

The photon detection efficiency has been studied using a control sample of $J/\psi \rightarrow \rho^0 \pi^0$ [40]. It is found that the difference between the detection efficiencies of data and MC is around 1% per photon. Thus, 2% is taken as the total systematic uncertainty for the detection of two photons in this analysis.

• Intermediate Decay Branching Fractions

The uncertainties of the quoted branching fractions for the intermediate particles ($\mathcal{B}(\Lambda \rightarrow p\pi^-)$, $\mathcal{B}(\pi^0 \rightarrow \gamma\gamma)$, and $\mathcal{B}(\eta \rightarrow \gamma\gamma)$) are taken from the PDG, and their uncertainties are considered as sources of systematic uncertainties.

8.1 $\psi(3686) \rightarrow \Lambda \bar{\Lambda} \pi^0$ systematic uncertainties

The additional systematic uncertainty may come from the following items:

• Mass Window Requirements

The systematic uncertainties associated with each invariant mass requirement are estimated by varying the size of the mass window by one standard deviation. The maximum resulting differences in branching fractions are considered as the systematic uncertainties for each requirement. By modifying each requirement, the maximum differences in branching fractions are presented in Table 11.

Mass window requirement	Change (MeV/ c^2)	Uncertainty (%)
$M(p\pi^-) \in (1.111, 1.121)\text{GeV}/c^2$	± 1	4.8
$M(\bar{p}\pi^+) \in (1.111, 1.121)\text{GeV}/c^2$	± 1	4.1
$M(\Lambda \bar{\Lambda}) < 3.4\text{GeV}/c^2$	-10	2.3
$M(\Lambda \bar{\Lambda}) \notin (3.077, 3.117)\text{GeV}/c^2$	+7	1.2
$M(\gamma_2 \Lambda / \gamma_2 \bar{\Lambda}) \notin (1.183, 1.203)\text{GeV}/c^2$	+3	0.2
$M_{\text{rec}}(\pi^+ \pi^-) \notin (3.087, 3.107)\text{GeV}/c^2$	+3	1.08
$M(p\pi^0 / \bar{p}\pi^0) \notin (1.17, 1.2)\text{GeV}/c^2$	+5	0.3

Tab. 11: Systematic uncertainties of each mass window requirement for $\psi(3686) \rightarrow \Lambda \bar{\Lambda} \pi^0$.

• Signal Shape

To obtain the number of π^0 events in the fit to $M(\gamma\gamma)$, the MC shape of the π^0 signal convolved with a Gaussian function is used to describe signal shape. In order to estimate the systematic uncertainty due to this shape, alternative fits are performed using a Breit-Wigner function convolved with a Gaussian function to determine the yields of the π^0 signal events. The maximum changes of 0.2% is taken as systematic uncertainties.

• Background

To estimate the uncertainty of non-peaking background, we performed alternative fits by replacing the first-order Chebychev polynomial with a second-order Chebychev polynomial. The maximum changes of **0.8%** is taken as systematic uncertainties.

Sources	Uncertainty(%)
Tracking Efficiency and $\Lambda(\bar{\Lambda})$ Reconstruction	1.1
Photon Detection Efficiency	2.0
Kinematic Fit	3.6
Mass Window Requirements	6.9
Signal Shape	0.2
Non-peaking Background	0.8
Peaking Background	1.5
$\mathcal{B}(\Lambda \rightarrow p\pi^-)$	0.8
$\mathcal{B}(\bar{\Lambda} \rightarrow \bar{p}\pi^+)$	0.8
$\mathcal{B}(\pi^0 \rightarrow \gamma\gamma)$	0.03
Physics model	1.1
Number of $\psi(3686)$ events	0.5
Total	8.45

Tab. 12: Systematic uncertainties of the branching fraction for $\psi(3686) \rightarrow \Lambda\bar{\Lambda}\pi^0$.

The uncertainty of peaking background is estimated by the fixing the number of continuum background. The uncertainty of peaking background from $\psi(3686) \rightarrow \bar{\Lambda}\Sigma^0\pi^0 + c.c.$ is estimated by fixing to its number of π^0 events with $\mathcal{B}(\psi(3686) \rightarrow \bar{\Lambda}\Sigma^0\pi^0 + c.c.)$ and MC detection efficiency. The maximum changes of **1.5%** is taken as systematic uncertainties.

- Physics Model

For the uncertainty from this physical model, the alternative model with PHSP with generator is used to determine the detection efficiency $\psi(3686) \rightarrow \Lambda\bar{\Lambda}\pi^0$. And the maximum change of the detection efficiency **1.1%** is taken as the systematic uncertainty.

All systematic uncertainties of the branching fraction for $\psi(3686) \rightarrow \Lambda\bar{\Lambda}\pi^0$ are summarized in

Table 12.

8.2 $\psi(3686) \rightarrow \Lambda\bar{\Lambda}\eta$ systematic uncertainties

Systematic uncertainties in the measurements of the branching fractions of intermediate resonances and the mass enhancement near $\Lambda\bar{\Lambda}$ threshold come from event selections and PWA.

• Mass Window Requirements

The systematic uncertainties associated with each mass window requirement are estimated by varying the size of the mass window by one standard deviation. The maximum resulting differences in branching fractions are considered as the systematic uncertainties for each requirement, as shown in Table 13.

Mass window requirement	Change (MeV/c ²)	Uncertainty (%)
$M(p\pi^-) \in (1.111, 1.121)\text{GeV}/c^2$	± 1	3.4
$M(\bar{p}\pi^+) \in (1.111, 1.121)\text{GeV}/c^2$	± 1	0.3
$M(\Lambda\bar{\Lambda}) < 3.077\text{GeV}/c^2$	+7	3.7
$M_{\text{rec}}(\pi^+\pi^-) \notin (3.087, 3.107)\text{GeV}/c^2$	+3	0.7

Tab. 13: Systematic uncertainties of mass window requirements for $\psi(3686) \rightarrow \Lambda\bar{\Lambda}\eta$.

• Signal Shape

To determine the number of η events by fitting to $M(\gamma\gamma)$, the Monte Carlo shape, convolved with a Gaussian function, is used to describe the η signal. To estimate the systematic uncertainty associated with the signal shape, alternative fitting procedures are performed by replacing the previous one with a Breit-Wigner function convolved with a Gaussian function. Then the maximum change of the branching fraction **1.1%** is taken as the systematic uncertainty.

• Background

The uncertainty related to the non-peaking background is estimated with a series of alternative fits. In these fits, the first-order Chebyshev polynomial function was substituted with a second-order Chebyshev polynomial for the $\psi(3686)$ data. The largest difference of **1.7%**, is taken as the systematic uncertainty.

The uncertainty of peaking background is estimated by fixing the number of QED continuum background with one statistical error. The maximum change of the branching fraction efficiency **1.2%** is taken as the systematic uncertainty.

• Physics Model

To better describe with $\psi(3686) \rightarrow \Lambda\bar{\Lambda}\eta$, an generator based on the PWA results is developed to deter-

mine the detection efficiency. For the uncertainty associated with this physical model, the $\Lambda(1670)$, $\Lambda(1800)$, and $\Lambda(2100)$ states are considered to determine the detection efficiency of $\psi(3686) \rightarrow \Lambda \bar{\Lambda} \eta$. The maximum change in the detection efficiency, **2.8%**, is taken as the systematic uncertainty.

Systematic uncertainties of the branching fraction for $\psi(3686) \rightarrow \Lambda \bar{\Lambda} \eta$ is summarized in Table 14.

Sources	Uncertainty (%)
Tracking Efficiency and $\Lambda(\bar{\Lambda})$ Reconstruction	1.1
Photon Detection Efficiency	2.0
Kinematic Fit	1.8
Mass Window Requirements	5.1
Signal Shape	1.1
Non-peaking Background	1.7
Peaking Background	1.2
$\mathcal{B}(\Lambda \rightarrow p\pi)$	0.8
$\mathcal{B}(\bar{\Lambda} \rightarrow \bar{p}\pi^+)$	0.8
$\mathcal{B}(\eta \rightarrow \gamma\gamma)$	0.5
Physics Model	2.8
Number of $\psi(3686)$ Events	0.5
Total	7.0

Tab. 14: Systematic uncertainties of the branching fraction for $\psi(3686) \rightarrow \Lambda \bar{\Lambda} \eta$.

Systematic Uncertainties from Partial Wave Analysis are considered as the following:

- Additional Resonance

To evaluate the effect on the PWA results from other possible components, PWA is re-performed by adding extra resonances $\Lambda(1810)$ or $\Lambda(1820)$, one at a time. The difference on branching fractions due to these additional resonances are taken as the systematic uncertainties.

- Background

The uncertainty of background is estimated by varying, the number of background events from non-peaking background and QED background with one statistical uncertainty, and the largest change of the results is assigned as the systematic uncertainty.

- Uncertainty from phase space

In TFPWA, $J^P = \frac{3}{2}^-$ phase space is considered. Due to the significant interference between $J^P = \frac{1}{2}^-$

phase space and the resonance states, the systematic uncertainty is estimated by replacing the $J^P = \frac{3}{2}^-$ phase space with $J^P = \frac{5}{2}^-$ phase space. The maximum resulting differences are taken as the systematic uncertainty.

- Fixed parameters

In the nominal fit, the mass and width values of the resonances are fixed to those of PDG. The systematic uncertainties is determined by changing these parameters with one statistical error in PWA, and the largest difference is taken as its uncertainty.

The systematic uncertainties on the PWA are summarized and listed in Table 15.

Source	FF of $\Lambda(1670)$	FF of $\Lambda(1800)$	FF of $\Lambda(2110)$
Additional Resonance	0.30	0.74	0.55
Background	10.22	15.66	12.58
PHSP	5.49	6.92	6.26
Mass	0.55	5.28	0.74
Width	0.12	5.72	0.30
Total	11.62%	18.82%	14.08%

Tab. 15: Systematic uncertainties for different sources from PWA.

Systematic Uncertainties for Mass and width of the threshold enhancement are considered as the following:

- Model of the threshold enhancement

In the fitting process, the mass threshold enhancement of $\Lambda\bar{\Lambda}$ is described using a relativistic Breit-Wigner model. The alternative Breit-Wigner formula for the $\Lambda\bar{\Lambda}$ mass structure is employed in PWA, the difference is taken as the uncertainty.

- Background

The uncertainty due to the non-peaking background is evaluated by varying the yields of the η side-band and deviating the continuum production from one times of its uncertainty. The largest difference is taken as the uncertainty.

- Event Selection

Uncertainty of event selection is discussed similar as the previous one and summarized Table 14.

The systematic uncertainties associated with the mass and width of the threshold enhancement, are given in Table 16.

Source	Mass(MeV)	Width (MeV)
Nominal	2291 ± 5	25 ± 8
Model of Threshold Enhancement	2	-
Background	4.7	2.3
Event Selection	3.7	6.7
Total	6.3	7.0

Tab. 16: Systematic uncertainty of mass and width for $\Lambda\bar{\Lambda}$ mass threshold.

9 Summary

Using a sample of $(2712 \pm 14) \times 10^8$ $\psi(3686)$ events collected with the BESIII detector, the decay of $\psi(3686) \rightarrow \Lambda\bar{\Lambda}\pi^0$ and $\psi(3686) \rightarrow \Lambda\bar{\Lambda}\eta$ are performed. The isospin symmetry breaking decay of $\psi(3686) \rightarrow \Lambda\bar{\Lambda}\pi^0$ is measured, and the corresponding branching fraction is determined to be $\mathcal{B}(\psi(3686) \rightarrow \Lambda\bar{\Lambda}\pi^0) = (0.93 \pm 0.15 \pm 0.08) \times 10^{-6}$.

PWA is performed to investigate the excited stated in the invariant mass of $\Lambda\eta(\bar{\Lambda}\eta)$. It is found that three intermediate resonances $\Lambda(1670)$, $\Lambda(1800)$, and $\Lambda(2110)$ are firstly observed in $\Lambda\eta$ system. The total branching fraction of is determined to be $(2.43 \pm 0.07 \pm 0.17) \times 10^{-5}$, and the branching fractions for the three resonances are firstly measured to be: $\mathcal{B}(\psi(3686) \rightarrow \Lambda(1670)\bar{\Lambda}) \times \mathcal{B}(\Lambda(1670) \rightarrow \Lambda\eta) + \text{c.c.} = (0.91 \pm 0.06 \pm 0.12) \times 10^{-5}$, $\mathcal{B}(\psi(3686) \rightarrow \Lambda(1800)\bar{\Lambda}) \times \mathcal{B}(\Lambda(1800) \rightarrow \Lambda\eta) + \text{c.c.} = (0.32 \pm 0.12 \pm 0.06) \times 10^{-5}$, and $\mathcal{B}(\psi(3686) \rightarrow \Lambda(2110)\bar{\Lambda}) \times \mathcal{B}(\Lambda(2110) \rightarrow \Lambda\eta) + \text{c.c.} = (0.46 \pm 0.05 \pm 0.07) \times 10^{-5}$, respectively.

In this analysis, an evident structure around the $\Lambda\bar{\Lambda}$ invariant mass threshold is observed for the first time in $\psi(3686) \rightarrow \Lambda\bar{\Lambda}\eta$, with a statistical significance of 4.85σ . Its mass and width are determined to be $(2291 \pm 5 \pm 6.3) \text{ MeV}/c^2$ and $(25 \pm 8 \pm 7.0) \text{ MeV}$ respectively, and its spin favors 1^{--} from PWA. Here the first uncertainty is statistical and the second is systematic. A future larger data sample is helpful to understand well the observed structure.

References

- [1] Luis Roca; Tetsuo Hyodo; Daisuke Jido, [Nucl.Phys.A809:65-87 \(2008\)](#).
- [2] [Chin. Phys. Lett. 39, 011201 \(2022\)](#).
- [3] J. Z. Bai et al. (BESIII Collaboration), [Phys. Rev. Lett. 91, 022001 \(2003\)](#).

- 499 [4] M. Ablikim et al. (BESIII Collaboration), [Phys. Rev. D 99, 032001 \(2019\)](#).
- 500 [5] M. Ablikim et al. (BESIII Collaboration), [Phys. Rev. D 97, 032013 \(2018\)](#).
- 501 [6] M. Ablikim et al. (BESIII Collaboration), [Phys. Rev. D 107, 112001 \(2023\)](#).
- 502 [7] Y. W. Chang et al. , (Belle Collaboration), [Phys. Rev. D 79, 052006 \(2009\)](#).
- 503 [8] B. Aubert et al. , (BaBar Collaboration), [Phys. Rev. D 79, 112009 \(2009\)](#).
- 504 [9] S. M. Gerasyuta and E. E. Matskevich, *Int. J. Mod. Phys. E* 29, 2050035 (2020).
- 505 [10] B.-D. Wan, S.-Q. Zhang, and C.-F. Qiao, [Phys. Rev. D 105 \(2022\)](#).
- 506 [11] [Chin. Phys. Lett. 39, 011201 \(2022\)](#).
- 507 [12] M. Ablikim et al. (BESIII Collaboration), [Phys. Rev. D 107, 112001 \(2023\)](#).
- 508 [13] M. Ablikim et al. (BESIII Collaboration), [Phys. Rev. D 104, 052006 \(2021\)](#).
- 509 [14] M. Ablikim et al. (BESIII Collaboration), [Phys. Rev. D 106, 072006\(2022\)](#).
- 510 [15] M. Ablikim et al. (BESIII Collaboration), [Nucl. Instrum. Methods Phys. Res., A 614, 345\[arXiv:0911.4960v1\]\[INSPIRE\]](#).
- 511
- 512 [16] C. Yu et al., (in Proc. of International Particle Accelerator Conference (IPAC'16)), [Busan, Korea, May 8-13, 2016, doi:10.18429/JACoW-IPAC2016-TUYA01](#).
- 513
- 514 [17] M. Ablikim et al. (BESIII Collaboration)], [Chin. Phys. C 44, \(2020\) 040001 \[arXiv:1912.05983\]](#)
- 515 [\[INSPIRE\]](#).
- 516 [18] P.Cao et al., [Nucl. Instrum. Meth. A 953, 163053 \(2020\)](#).
- 517 [19] M. Ablikim et al., [arXiv:2403.06766\[hep-ex\]](#).
- 518 [20] M. Ablikim et al., [arXiv:1507.08188 \[hep-ex\]](#).
- 519 [21] M. Ablikim et al., [arXiv:2406.05827 \[hep-ex\]](#).
- 520 [22] S. Agostinelli et al. [GEANT4], [Nucl. Instrum. Meth. A 506, 250-303 \(2003\)](#).
- 521 [23] S. Jadach, B. F. L. Ward and Z. Was, [Comput. Phys. Commun. 130, \(2000\) 260](#).
- 522 [24] S. Jadach, B. F. L. Ward and Z. Was, [Phys. Rev. D 63, 113009 \(2001\)](#).

- [25] D. J. Lange, *Nucl. Instrum. Meth. A* **462**, 152 (2001).
- [26] R. G. Ping, *Chin. Phys. C* **32**, (2008) 599.
- [27] P. A. Zyla et al. ,[Particle Data Group], *Phys. Rev. D* **110**, 030001 (2024).
- [28] J. C. Chen, G. S. Huang, X. R. Qi, D. H. Zhang and Y. S. Zhu, *Phys. Rev. D* **62**, 034003 (2000).
- [29] R. L. Yang, R. G. Ping and H. Chen, *Chin. Phys. Lett.* **31**, 061301 (2014).
- [30] E. Richter-Was, *Phys. Lett. B* **303**, 163 (1993).
- [31] X. Zhou, S. Du, G. Li and C. Shen, *Comput. Phys. Commun.* **258**, 107540 (2021).
- [32] M. Ablikim et al. (BESIII Collaboration), *Phys. Rev. D* **106**, 072006 (2022).
- [33] Y. Jiang et al., Open-source framework TF-PWA package, GitHub link:
<https://github.com/jiangyi15/tf-pwa> (2020).
- [34] S.U. Chung, A General formulation of covariant helicity coupling amplitudes, *Phys. Rev. D* **57** (1998).
- [35] F. Von Hippel and C. Quigg, Centrifugal-barrier effects in resonance partial decay widths, shapes, and production amplitudes, *Phys. Rev. D* **5** (1972).
- [36] M. Wang, Y. Jiang, Y. Liu, W. Qian, X. Lyu and L. Zhang, A novel method to test particle ordering and final state alignment in helicity formalism, *Chin. Phys. C* **45** (2021) 063103 [arXiv:2012.03699] [INSPIRE].
- [37] BESIII collaboration, *Phys. Rev. D* **101**, 032008 (2020).
- [38] C. Langenbruch, Parameter uncertainties in weighted unbinned maximum likelihood fits, *Eur. Phys. J. C* **82** (2022) 393.
- [39] BESIII collaboration, Study of J/ψ and ψ decay to $\Lambda\bar{\Lambda}$ and $\Sigma^0\bar{\Sigma}^0$ final states, *Phys. Rev. D* **95**, 052003 (2017).
- [40] M. Ablikim et al. (BESIII Collaboration), *Phys. Rev. D* **83**, 112005 (2011).

546

10 Appendices

rowNo	decay tree	decay final state	iDcyTr	nEtr	nCEtr
1	$\psi' \rightarrow \pi^0 \Lambda \bar{\Lambda}, \Lambda \rightarrow \pi^- p, \bar{\Lambda} \rightarrow \pi^+ \bar{p}$	$\pi^0 \pi^+ \pi^- p \bar{p}$	1	4814	4814
2	$\psi' \rightarrow \Lambda \bar{\Lambda} \gamma, \Lambda \rightarrow \pi^- p, \bar{\Lambda} \rightarrow \pi^+ \bar{p}$	$\pi^+ \pi^- p \bar{p} \gamma$	3	198	5012
3	$\psi' \rightarrow \pi^0 \Delta^{++} \bar{\Delta}^{--}, \Delta^{++} \rightarrow \pi^+ p, \bar{\Delta}^{--} \rightarrow \pi^- \bar{p}$	$\pi^0 \pi^+ \pi^- p \bar{p}$	0	94	5106
4	$\psi' \rightarrow \bar{\Lambda} \Sigma^{*0}, \bar{\Lambda} \rightarrow \pi^+ \bar{p}, \Sigma^{*0} \rightarrow \pi^0 \Lambda, \Lambda \rightarrow \pi^- p$	$\pi^0 \pi^+ \pi^- p \bar{p}$	6	30	5136
5	$\psi' \rightarrow \Lambda \bar{\Sigma}^{*0}, \Lambda \rightarrow \pi^- p, \bar{\Sigma}^{*0} \rightarrow \pi^0 \bar{\Lambda}, \bar{\Lambda} \rightarrow \pi^+ \bar{p}$	$\pi^0 \pi^+ \pi^- p \bar{p}$	7	29	5165
6	$\psi' \rightarrow \pi^0 \pi^+ \pi^- p \bar{p}$	$\pi^0 \pi^+ \pi^- p \bar{p}$	2	23	5188
7	$\psi' \rightarrow \Lambda \bar{\Sigma}^0 \gamma, \Lambda \rightarrow \pi^- p, \bar{\Sigma}^0 \rightarrow \bar{\Lambda} \gamma, \bar{\Lambda} \rightarrow \pi^+ \bar{p}$	$\pi^+ \pi^- p \bar{p} \gamma \gamma$	10	19	5207
8	$\psi' \rightarrow \chi_{c1} \gamma, \chi_{c1} \rightarrow \pi^0 \Lambda \bar{\Lambda}, \Lambda \rightarrow \pi^- p, \bar{\Lambda} \rightarrow \pi^+ \bar{p}$	$\pi^0 \pi^+ \pi^- p \bar{p} \gamma$	5	12	5219
9	$\psi' \rightarrow \bar{\Lambda} \Sigma^0 \gamma, \bar{\Lambda} \rightarrow \pi^+ \bar{p}, \Sigma^0 \rightarrow \Lambda \gamma, \Lambda \rightarrow \pi^- p$	$\pi^+ \pi^- p \bar{p} \gamma \gamma$	4	11	5230
10	$\psi' \rightarrow \chi_{c2} \gamma, \chi_{c2} \rightarrow \pi^0 \Lambda \bar{\Lambda}, \Lambda \rightarrow \pi^- p, \bar{\Lambda} \rightarrow \pi^+ \bar{p}$	$\pi^0 \pi^+ \pi^- p \bar{p} \gamma$	18	10	5240
11	$\psi' \rightarrow \pi^0 \Lambda \bar{\Sigma}^0, \Lambda \rightarrow \pi^- p, \bar{\Sigma}^0 \rightarrow \bar{\Lambda} \gamma, \bar{\Lambda} \rightarrow \pi^+ \bar{p}$	$\pi^0 \pi^+ \pi^- p \bar{p} \gamma$	11	9	5249
12	$\psi' \rightarrow \pi^0 \bar{\Lambda} \Sigma^0, \bar{\Lambda} \rightarrow \pi^+ \bar{p}, \Sigma^0 \rightarrow \Lambda \gamma, \Lambda \rightarrow \pi^- p$	$\pi^0 \pi^+ \pi^- p \bar{p} \gamma$	13	7	5256
13	$\psi' \rightarrow \chi_{c0} \gamma, \chi_{c0} \rightarrow \Lambda \bar{\Lambda}, \Lambda \rightarrow \pi^- p, \bar{\Lambda} \rightarrow \pi^+ \bar{p}$	$\pi^+ \pi^- p \bar{p} \gamma$	21	6	5262
14	$\psi' \rightarrow \pi^0 \Delta^0 \bar{\Delta}^0, \Delta^0 \rightarrow \pi^- p, \bar{\Delta}^0 \rightarrow \pi^+ \bar{p}$	$\pi^0 \pi^+ \pi^- p \bar{p}$	17	4	5266

Tab. 17: Decay trees and their respective final states

rowNo	decay tree	decay final state	iDcyTr	nEtr	nCEtr
1	$\psi' \rightarrow \Lambda \bar{\Sigma}^0 \gamma, \Lambda \rightarrow \pi^- p, \bar{\Sigma}^0 \rightarrow \bar{\Lambda} \gamma, \bar{\Lambda} \rightarrow \pi^+ \bar{p}$	$\pi^+ \pi^- p \bar{p} \gamma \gamma$	1	411	411
2	$\psi' \rightarrow \bar{\Lambda} \Sigma^0 \gamma, \bar{\Lambda} \rightarrow \pi^+ \bar{p}, \Sigma^0 \rightarrow \Lambda \gamma, \Lambda \rightarrow \pi^- p$	$\pi^+ \pi^- p \bar{p} \gamma \gamma$	0	388	799
3	$\psi' \rightarrow \eta \Lambda \bar{\Lambda}, \eta \rightarrow \gamma \gamma, \Lambda \rightarrow \pi^- p, \bar{\Lambda} \rightarrow \pi^+ \bar{p}$	$\pi^+ \pi^- p \bar{p} \gamma \gamma$	4	67	866
4	$\psi' \rightarrow \Sigma^0 \bar{\Sigma}^0 \gamma, \Sigma^0 \rightarrow \Lambda \gamma, \bar{\Sigma}^0 \rightarrow \bar{\Lambda} \gamma, \Lambda \rightarrow \pi^- p, \bar{\Lambda} \rightarrow \pi^+ \bar{p}$	$\pi^+ \pi^- p \bar{p} \gamma \gamma \gamma$	2	55	921
5	$\psi' \rightarrow \chi_{c0} \gamma, \chi_{c0} \rightarrow \pi^0 \Lambda \bar{\Lambda}, \Lambda \rightarrow \pi^- p, \bar{\Lambda} \rightarrow \pi^+ \bar{p}$	$\pi^0 \pi^+ \pi^- p \bar{p} \gamma$	3	31	952
6	$\psi' \rightarrow \chi_{c1} \gamma, \chi_{c1} \rightarrow \pi^0 \Lambda \bar{\Lambda}, \Lambda \rightarrow \pi^- p, \bar{\Lambda} \rightarrow \pi^+ \bar{p}$	$\pi^0 \pi^+ \pi^- p \bar{p} \gamma$	16	19	971
7	$\psi' \rightarrow \eta_c \gamma, \eta_c \rightarrow \Lambda \bar{\Sigma}^0, \Lambda \rightarrow \pi^- p, \bar{\Sigma}^0 \rightarrow \bar{\Lambda} \gamma, \bar{\Lambda} \rightarrow \pi^+ \bar{p}$	$\pi^+ \pi^- p \bar{p} \gamma \gamma$	10	18	989
8	$\psi' \rightarrow \chi_{c2} \gamma, \chi_{c2} \rightarrow \pi^0 \Lambda \bar{\Lambda}, \Lambda \rightarrow \pi^- p, \bar{\Lambda} \rightarrow \pi^+ \bar{p}$	$\pi^0 \pi^+ \pi^- p \bar{p} \gamma$	17	16	1005
9	$\psi' \rightarrow \eta' p \bar{p}, \eta' \rightarrow \pi^+ \pi^- \eta, \eta \rightarrow \gamma \gamma$	$\pi^+ \pi^- p \bar{p} \gamma \gamma$	18	12	1017
10	$\psi' \rightarrow \pi^0 \bar{\Lambda} \Sigma^0, \bar{\Lambda} \rightarrow \pi^+ \bar{p}, \Sigma^0 \rightarrow \Lambda \gamma, \Lambda \rightarrow \pi^- p$	$\pi^0 \pi^+ \pi^- p \bar{p} \gamma$	6	11	1028
11	$\psi' \rightarrow \eta_c \gamma, \eta_c \rightarrow \bar{\Lambda} \Sigma^0, \bar{\Lambda} \rightarrow \pi^+ \bar{p}, \Sigma^0 \rightarrow \Lambda \gamma, \Lambda \rightarrow \pi^- p$	$\pi^+ \pi^- p \bar{p} \gamma \gamma$	7	11	1039
12	$\psi' \rightarrow \pi^0 \Lambda \bar{\Sigma}^0, \Lambda \rightarrow \pi^- p, \bar{\Sigma}^0 \rightarrow \bar{\Lambda} \gamma, \bar{\Lambda} \rightarrow \pi^+ \bar{p}$	$\pi^0 \pi^+ \pi^- p \bar{p} \gamma$	24	5	1044
13	$\psi' \rightarrow \eta_c \gamma, \eta_c \rightarrow \Sigma^0 \bar{\Sigma}^0, \Sigma^0 \rightarrow \Lambda \gamma, \bar{\Sigma}^0 \rightarrow \bar{\Lambda} \gamma, \Lambda \rightarrow \pi^- p, \bar{\Lambda} \rightarrow \pi^+ \bar{p}$	$\pi^+ \pi^- p \bar{p} \gamma \gamma \gamma$	29	5	1049
14	$\psi' \rightarrow \chi_{c2} \gamma, \chi_{c2} \rightarrow \Lambda \bar{\Lambda} \gamma, \Lambda \rightarrow \pi^- p, \bar{\Lambda} \rightarrow \pi^+ \bar{p}$	$\pi^+ \pi^- p \bar{p} \gamma \gamma$	23	4	1053
15	$\psi' \rightarrow \pi^0 \Sigma^0 \bar{\Sigma}^0, \Sigma^0 \rightarrow \Lambda \gamma, \bar{\Sigma}^0 \rightarrow \bar{\Lambda} \gamma, \Lambda \rightarrow \pi^- p, \bar{\Lambda} \rightarrow \pi^+ \bar{p}$	$\pi^0 \pi^+ \pi^- p \bar{p} \gamma \gamma$	34	4	1057
16	$\psi' \rightarrow \pi^0 J/\psi, J/\psi \rightarrow \Lambda \bar{\Lambda} \gamma, \Lambda \rightarrow \pi^- p, \bar{\Lambda} \rightarrow \pi^+ \bar{p}$	$\pi^0 \pi^+ \pi^- p \bar{p} \gamma$	25	3	1060
17	$\psi' \rightarrow \chi_{c1} \gamma, \chi_{c1} \rightarrow J/\psi \gamma, J/\psi \rightarrow \Lambda \bar{\Lambda} \gamma, \Lambda \rightarrow \pi^- p, \bar{\Lambda} \rightarrow \pi^+ \bar{p}$	$\pi^+ \pi^- p \bar{p} \gamma \gamma \gamma$	26	3	1063
18	$\psi' \rightarrow \chi_{c2} \gamma, \chi_{c2} \rightarrow J/\psi \gamma, J/\psi \rightarrow \Lambda \bar{\Lambda} \gamma, \Lambda \rightarrow \pi^- p, \bar{\Lambda} \rightarrow \pi^+ \bar{p}$	$\pi^+ \pi^- p \bar{p} \gamma \gamma \gamma$	8	2	1065
19	$\psi' \rightarrow \pi^0 \Lambda \bar{\Lambda} \gamma, \Lambda \rightarrow \pi^- p, \bar{\Lambda} \rightarrow \pi^+ \bar{p}$	$\pi^0 \pi^+ \pi^- p \bar{p} \gamma$	28	2	1067
20	$\psi' \rightarrow \chi_{c1} \gamma, \chi_{c1} \rightarrow J/\psi \gamma, J/\psi \rightarrow \Lambda \bar{\Lambda}, \Lambda \rightarrow \pi^- p, \bar{\Lambda} \rightarrow \pi^+ \bar{p}$	$\pi^+ \pi^- p \bar{p} \gamma \gamma$	5	2	1069

Tab. 18: Decay Trees and Final States